TÉCNICO LISBOA

Aerodynamic Characterization of UAV Propellers Using Numerical Analysis and Experimental Testing

Gonçalo Filipe Vizeu

Thesis to obtain the Master of Science Degree in

Aerospace Engineering

Supervisors: Prof. André Calado Marta
Prof. Pietro Paolo Ciottoli

Examination Committee

Chairperson: Prof. João Manuel Melo de Sousa
Supervisor: Prof. André Calado Marta
Member of the Committee: Prof. João Eduardo De Barros Teixeira Borges

December 2023

Declaration

I declare that this document is an original work of my own authorship and that it fulfills all the requirements of the Code of Conduct and Good Practices of the Universidade de Lisboa.

Resumo

Nas últimas décadas houve grandes desenvolvimentos tecnológicos em Veículos Aéreos Não-Tripulados (VANTs) e, nos dias de hoje, estes são utilizados para uma ampla gama de aplicações comercias, como monitorização de trânsito e metereologia, realização de serviços de entrega e deteção de incêndios florestais. Este trabalho apresenta e compara diferentes análises numéricas de baixa-fidelidade e alta-fidelidade que prevêem o desempenho de um hélice de um VANT para diferentes configurações de voo. Primeiramente, a força propulsiva e torque de dois hélices comerciais são obtidos recorredo ao software JavaProp, um software baseado na Teoria do Elemento de Pá. Por fim, uma análise dinâmica de fluidos computacional é realizada no software comercial ANSYS® Fluent® que inclui também a construção do modelo CAD dos hélices e modelação do domínio do escoamento. Paralelamente, estudos relacionados com o modelo de turbulência e refinamento da malha são conduzidos e as performances dos dois hélices comerciais são determinadas para diferentes escoamentos e condições de voo. Por fim, uma análise experimental é conduzida para um dos hélices comerciais e os resultados são validados com simulações computacionais. As descobertas deste estudo sugerem que a análise computacional de alta-fidelidade fornece resultados mais consistentes com os ensaios experimentais, enquanto a precisão dos resultados derivados da Teoria do Elemento de Pá diminui com o aumento da velocidade de rotação do hélice. No entanto, ambos os métodos mostram-se adequados para prever o desempenho do hélice em diferentes cenários de voo.

Palavras-chave: Hélice, Dinâmica de Fluidos Computacional, Teoria do Elemento de Pá, Força Propulsiva, Torque, Validação

Abstract

Over the last decades, there have been major developments in Unmanned Aerial Vehicles (UAVs) and, nowadays, they are used for a wide range of commercial applications such as traffic and weather monitoring, deliveries and forest fire detection. This study presents and compares different low-fidelity and high-fidelity aerodynamic numerical models that predict the performance of a UAV propeller for a wide range of flight conditions, such as hovering and vertical climbing. First, the thrust and torque of two commercial propellers are obtained recurring to JavaProp, a software based on the Blade Element Theory. Then, computational fluid dynamics analysis is carried out in the commercial software ANSYS® Fluent®, which includes the construction of the CAD model of the propellers and the flow domain modeling. Furthermore, turbulence model and mesh studies were conducted and the propeller thrust and torque were determined for different flight configurations and flow conditions. Finally, experimental testing to evaluate the aerodynamic performance of one propeller was conducted and the results were validated with computational simulations. The findings of this study suggest that high-fidelity computational models provide results more consistent with experimental testing, whereas the accuracy of results derived from the low-fidelity Blade Element Theory decreases with increasing the propeller angular velocity. Nevertheless, both methods are shown to be suitable for forecasting propeller performance in various flow and flight scenarios.

Keywords: Propeller Design, CFD, Blade Element Theory, Thrust, Torque, Validation

Contents

List of Tables

List of Figures

Nomenclature

Greek symbols

α	Angle of attack
α_i	Induced angle of attack
β	Pitch angle
η	Propeller efficiency
μ	Molecular viscosity coefficient
ν	Kinematic Viscosity
Ω	Angular velocity of the propellerp
ρ	Density

Roman symbols

B	Number of blades
c	Chord
C_D	Coefficient of drag
C_L	Coefficient of lift
C_M	Coefficient of moment
C_P	Power coefficient
C_Q	Torque coefficient
C_T	Thrust coefficient
D	Drag
E	Energy
e	Specific Energy
H	Enthalpy

h	Specific Enthalpy
I	Current
J	Advance ratio
L	Lift
n	Angular Velocity (RPM)
P	Power
p	Pressure
Q	Torque
r	Radius
S	Strain-Rate Stress Tensor
T	Thrust
V	Velocity
$V*$	Voltage
w	Induced velocity
$y*$	Non-Dimensional Height from the Propeller Wall within the Boundary Layer
$y+$	Non-Dimensional Height of the First Layer of the Boundary Layer

Subscripts

∞	Free-stream condition
i, j, k	Computational indexes
n	Normal component
x, y, z	Cartesian components
ref	Reference condition

Glossary

APC Advanced Precision Propellers

ARS Algebraic Reynolds-Stress

BEMT Blade Element Momentum Theory

BET Blade Element Theory

CAD Computer-Aided Design

CFD Computational Fluid Dynamics

DNS Direct Numerical Simulation

ESC Electronic Speed Control

IST Instituto Superior Técnico

LES Large-Eddy Simulation

MPM Mixing Plane Model

MRF Multiple Reference Frame

PMW Pulse Width Modulation

RANS Reynolds-Averaged Navier-Stokes

RPM Rotations Per Minute

RST Reynolds-Stress Transport

SIMPLE Semi-Implicit Method for Pressure Linked Equations

SST Shear-Stress Transport

STC Self-Temperature Compensation

UAV Unmanned Aerial Vehicle

UIUC University of Illinois at Urbana-Champaign

VTOL Vertical Take Off and Landing

Chapter 1

Introduction

1.1 Motivation

Unmanned Aerial Vehicles (UAV), also known as drones, are types of aircraft that can be remotely controlled or fly autonomously by software-controlled flight plans in their embedded systems.

The first developments in UAVs occurred in the mid-1990s and came through the United States Army, as these devices were used for vigilance and survey missions. The use of UAVs for civil and commercial applications came later due to their high costs and the complexity of missions. Due to their exorbitant expenses and intricate assignments, UAVs were once exclusively reserved for military use. Nevertheless, in recent times, UAVs have garnered considerable attention for their diverse commercial applications. An instance of UAV use is the plan announced by Amazon in 2013 to make deliveries through drones on a recurring basis. Drones are also utilized for various purposes, such as weather and traffic monitoring and forest fire detection. As battery life improves and flight components such as sensors and processors advance, there is a growth in the areas where UAVs are employed.

UAVs are classified according to their features, such as maximum altitude, wingspan size, weight, and flight range, among others. Two main types of UAVs are being studied nowadays: fixed-wing and rotary-wing, as shown in Figure 1.1.

(a) Fixed-Wing UAV. [1]

(b) Rotary-wing UAV. [2]

Figure 1.1: Types of UAVs.

Fixed-wing UAVs have a similar build to airplanes and make use of aerodynamic lift from their structure, requiring less energy to stay in the air. This allows them to fly for longer periods than other UAVs. However, they need ample space for take-off and landing and cannot hover.

Finally, rotary wings are the most cost-effective option on the UAV market and are classified by the number of rotors they have: tricopter (3 rotors), quadrocopter (4 rotors), hexacopter (6 rotors), and more. These rotors can produce thrust hence, the amount of payload that a rotary wing can carry increases with the number of rotors. VTOL (Vertical Take Off and Landing) and hovering are the most notable differences between rotary wings and other types of UAVs. High maneuverability and VTOL capability enable rotary wings to handle challenging tasks in challenging conditions. However, the payload capacity of most UAVs is insufficient to carry heavy components and materials. Hence, the aerodynamic performance and the geometric characteristics can be analyzed and studied to improve the payload capacity and performance of rotary-wing UAVs.

As previously mentioned, rotary-wing UAVs are used for a wide range of applications in the health, security, agriculture and military fields, among others. This means that accuracy is key when analyzing the UAV propellers' performance for the different flow conditions in flight operations. The most reliable way of evaluating a propeller's performance is through experimental testing. Static tests can be performed without a wind tunnel and are relatively cheap, but dynamic tests that represent better the real conditions of a flight require more expensive equipment. Another problem associated with the experimental testing of a propeller comes with the need for physical geometry. This becomes a problem when the objective is the optimization of the propeller design, as every little change in the geometry will require the production and manufacturing of a new propeller and a consequent increase in cost and time.

Different numerical methods have been developed in the last century to predict the performance of a rotary-wing propeller. More straightforward approaches like the Blade Element Theory (BET) are relatively accurate for low values of the Reynolds number. On the other hand, CFD (Computational Fluid Dynamics) simulations are able to represent suitably the flow field around the propeller and, therefore, to predict its performance. Some of these methods and approaches will be studied in this work.

1.2 Literature Review

A UAV's primary component is the propeller, composed of a rotating hub and radiating blades that are set at a pitch to form a helical spiral that, when rotated, performs an action that is similar to Archimedes' screw. Propellers are identified by their diameter and pitch, with size measured in inches. For instance, a 14"x13" propeller has a diameter of 14 inches and a pitch of 13 inches. Small-diameter propellers have a diameter in the range of 6 to 22 inches, and operate at low Reynolds numbers, typically between 30000 and 300000 [3].

The geometry of a propeller consists of various elements that play a crucial role in its operation [4]. Figure 1.2 provides a detailed view of these elements, including the hub which attaches the propeller blades to the power source, the leading edge which is the first point of contact with the fluid flow line, and the trailing edge which is the element that ultimately interacts with the fluid flow line. Additionally, the

pitch angle β is the angle at which each station of the blade is rotated relative to the propeller disk plane. The diameter of the disk is defined by the rotating propeller, and the chord length, c, is the distance between the leading and trailing edges.

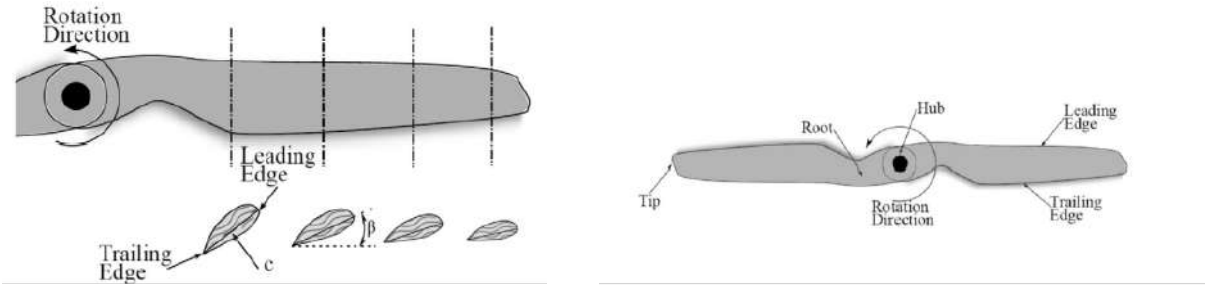

(a) Propeller blade cross sections. (b) Propeller geometry.

Figure 1.2: Propeller blade cross sections and geometry. [4]

In recent decades, there has been a significant increase in interest in UAVs, which has led to a greater focus on rotary wing aerodynamics. As a result, there have been numerous advancements made in propeller design for air vehicles. As such, ongoing studies continue to explore the aerodynamic, performance, and structural aspects of propellers.

As explained in the previous Section, there are different methods to predict the performance of a propeller. These methods can be experimental or numerical. In their experimental study, J. B. Brandt and M. S. Selig [5] made thrust and torque measurements of 79 commercial propellers that are used on small UAVs. The experiments were carried out in a subsonic wind tunnel with a rectangular cross-section of 0.853×1.219 meters and length equal to 2.438 meters at the University of Illinois at Urbana-Champaign (UIUC), as shown in Figure 1.3.

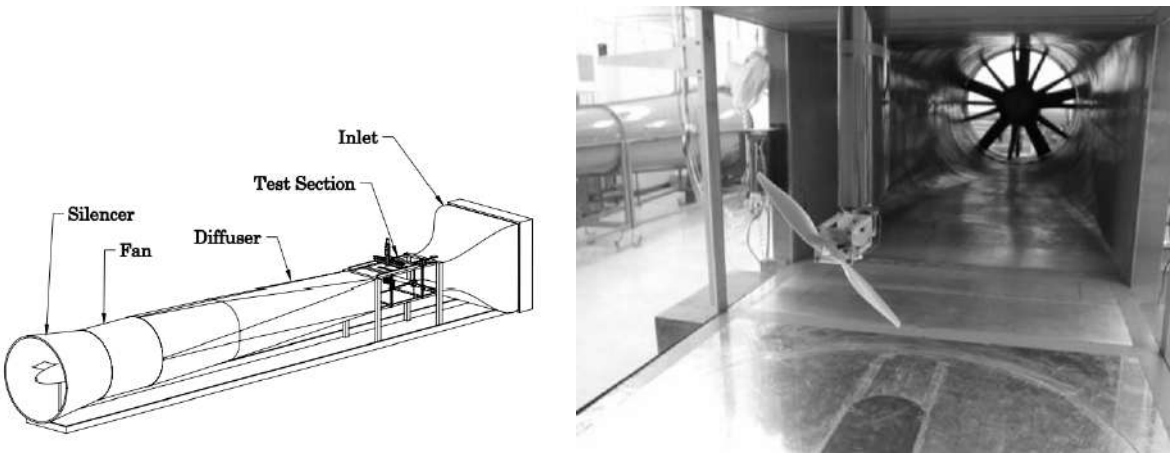

(a) UIUC subsonic wind tunnel. (b) Test section with experimental equipment installed.

Figure 1.3: Experimental testing: Wind tunnel at UIUC. [6]

The experimental setup consists of a mechanism that hangs into the tunnel from the ceiling. The thrust and the torque produced by a clockwise rotating propeller are shown in Figure 1.4.

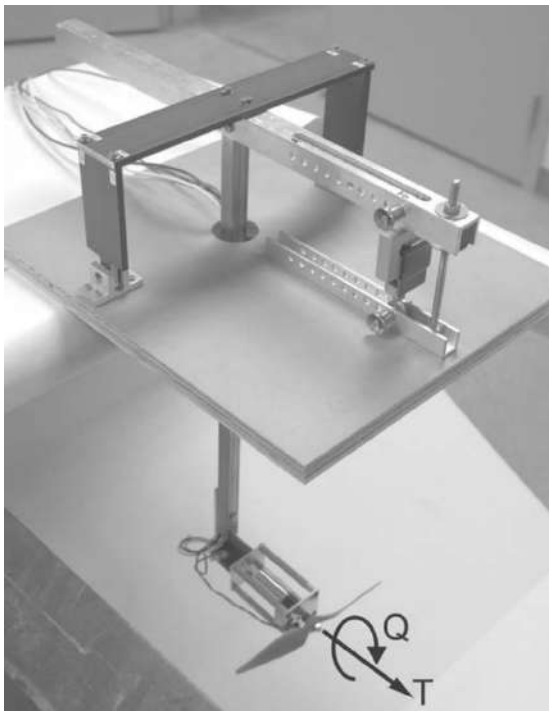

Figure 1.4: Experimental setup: thrust measurement. [6]

The thrust measurement mechanism is a simple T-shaped structure that pivots about two flexible pivots and is constrained by a load cell that sits outside of the tunnel.

Moreover, the torque produced by the propeller is measured by torque transducers that are placed between the motor housing and the support arm of the thrust mechanism, as shown in Figure 1.5.

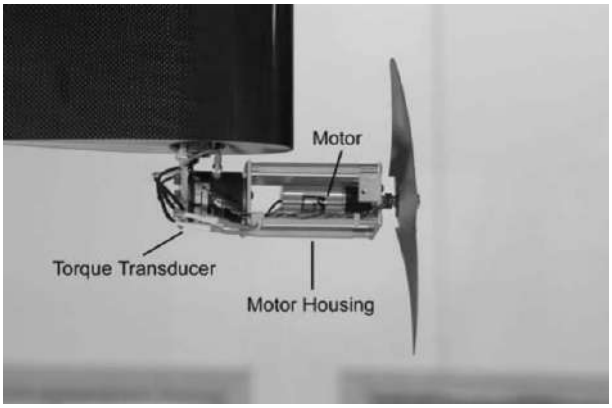

Figure 1.5: Experimental setup: torque measurement. [6]

The data on 79 commercial propellers can be found in [7]. This thesis aims to analyze and compare the performance of two commercial propellers using analytical methods and compare them with the experimental testing carried out at UIUC. Other experimental studies were conducted in [8–10].

Numerical methods have been documented to predict the performance of propellers, primarily in the marine industry, alongside experimental testing. One example is E. Benini's comparison of two analysis methods in [11]. The combined Blade Element Momentum Theory's (BEMT) results were

validated against experimental data, and then compared to the results of a 3D CFD analysis conducted in ANSYS® Fluent®. Although both methods were reliable, the CFD analysis was found to be more accurate compared to the first method. A similar analysis comparison was conducted by J. Carroll [12]. Moreover, D. Wilhelm [13] presented an overview of steady-state and unsteady CFD simulations for many rotating flow systems, using OpenFOAM® software. In this paper, a comparison between BEMT and steady-state and unsteady CFD simulations models for a small low-Reynolds propeller is presented.

Other CFD simulations have been reported, but they often focus on hovering scenarios with zero free stream velocity. H. Kutty and P. Rajendran [14] conducted an advancing flow analysis using an unstructured mesh and a moving reference frame to simulate the rotation of the APC 10”x7” Slow Flyer commercial propeller.

1.3 Objectives and Thesis Outline

The aim of this Thesis is to explore and compare various methods and approaches for predicting the performance of a rotating propeller in different flight and flow configurations. These methods are categorized as either low-fidelity or high-fidelity numerical analyses based on their level of complexity. The investigation will focus on the performance of two commercial propellers, namely the APC 14”x13” Sport and APC 10”x8” Sport, at different rotational and free stream velocities.

This Thesis comprises six chapters. Chapter 1 provides a brief introduction to the topic, as well as the motivation and objectives of the work. Chapter 2 outlines the different techniques used to determine a rotating propeller’s performance, categorized as low-fidelity or high-fidelity. The Chapter further delves into the Actuator Disc Theory and Blade Element Theory. Additionally, the numerical methods used by ANSYS® Fluent® to simulate the flow characteristics around a rotating propeller are described, including the turbulence models and the spatial discretization of the domain.

Chapter 3 covers the numerical methodology used to analyze commercial propellers. This section details the formulation of the flow domain around the propeller and outlines the process of creating an accurate CAD model of real commercial propellers using SolidWorks®.

In Chapter 4, various numerical studies will be conducted on the two commercial propellers being studied. These studies will include mesh refinement and turbulence model analysis with the goal of identifying the most suitable model or mesh for each propeller and flow condition. The outcomes of low and high-fidelity numerical techniques will be analyzed and discussed to determine their performance.

Chapter 5 provides a detailed explanation of the experimental methodology and setup for the propeller test instruments, including their design. The Chapter also covers the aerodynamic performance results that will be obtained through experimentation for the APC 10”x8” Sport propeller. Finally, Chapter 6 concludes the study by presenting its major findings.

Chapter 2

Propeller Analysis Models

This Chapter discusses analytical and numerical approaches for estimating slipstream characteristics in propeller flow. Over the past few decades, there have been significant advancements in propeller theories. Nowadays, there are various methods available for propeller design and analysis, offering different levels of sophistication.

In Sections 2.1 and 2.2, two theoretical approaches are explored for determining a propeller's aerodynamic performance. Blade Element and Actuator Disc theories are considered low-fidelity numerical techniques used to calculate steady-state flow over propellers. However, these methods may not be accurate for extreme flow conditions and therefore require validation through experimental data.

Moreover, in the remaining sections, an overview of different methods embedded in the commercial CFD software ANSYS® Fluent® will be given to model rotating flows, specifically the flow around small-scale propellers at low Reynolds numbers.

With advancements in computer technology, CFD methods have become a valuable tool for analyzing propeller designs. Turbulence modeling is essential in most CFD simulations to accurately determine flow properties, as most engineering problems involve turbulence. Various methods, such as Reynolds-Averaged Navier-Stokes (RANS), have been studied and proven to predict flow properties with accuracy in propeller case studies. These methods are high-fidelity numerical techniques based on mathematical models.

2.1 Actuator Disc Theory

The Integral Momentum Theory, also called the Disc Actuator Theory, serves as a fundamental model for projecting a propeller's functioning under varying conditions, including changes in altitude, temperature, or air density. Rankine was the first to introduce this theory, which was later expanded upon by Froude [15]. Though initially designed for marine propellers, the propeller is simulated as an infinitely thin permeable disc with the same diameter as its blades. By applying the Bernoulli equation and equilibrium of forces, the propeller's performance parameters can be ascertained. This model, presented in Figure 2.1, considers the assumptions of constant velocity and uniform pressure over the

disc, inviscid and incompressible fluid and stationary and irrotational flow.

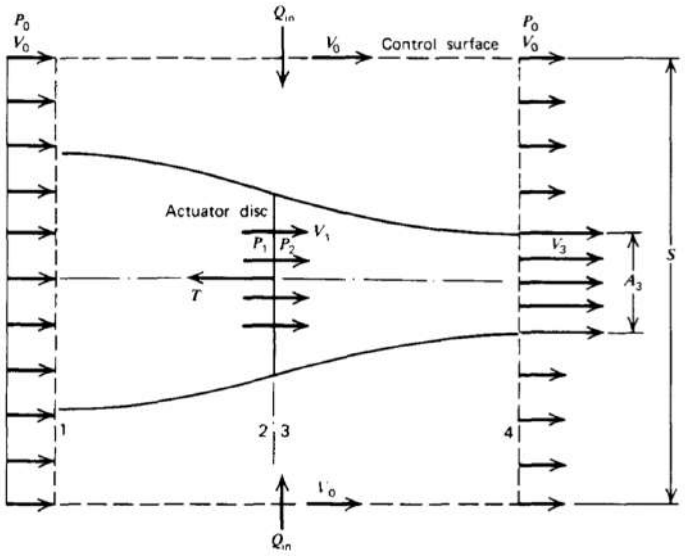

Figure 2.1: Idealized flow model for disc actuator theory. [15]

Recalling Newton's second law that a control volume of fixed mass can be written to relate external forces to changes in momentum,

$$\sum \vec{F} = \vec{a_0} \int_V \rho \, dV + \int_V \rho \frac{D\vec{U}}{Dt} \, dV \ , \tag{2.1}$$

where the first term is the sum of all external forces applied to the volume, the second term corresponds to forces due to a change in inertia and the third term is the change in the momentum of mass of the control volume. Applying the previous law to the model presented in Figure 2.1 and its assumptions, thrust becomes

$$T = \dot{m}(V_3 - V). \tag{2.2}$$

Considering the continuity of the flow along the stream tube, yields

$$\dot{m} = \rho A_3 V_3. \tag{2.3}$$

The thrust T is also equal to the pressure difference across the actuator disc given by

$$T = \int \int_{disc} p \, dS = \Delta p A_{disc} = A_{disc}(p_2 - p_1). \tag{2.4}$$

As one of the assumptions of the Disc Actuator Theory is the flow incompressibility, this allows the application of Bernoulli's Theorem along any streamline. Hence, pressures p_1 and p_2 are related by application of such theorem upstream and downstream of the propeller, resulting

$$p_0 + \frac{1}{2}\rho V^2 = p_1 + \frac{1}{2}\rho V_1^2 \tag{2.5}$$

and

$$p_0 + \frac{1}{2}\rho V_3^2 = p_2 + \frac{1}{2}\rho V_2^2. \tag{2.6}$$

Subtracting Equations (2.5) from (2.6) and noting that the velocity is continuous through the propeller:

$$p_2 - p_1 = \frac{1}{2}\rho(V_3^2 - V^2). \tag{2.7}$$

Combining Equations (2.2), (2.3), (2.4) and (2.7) and using the fact from continuity that $A_3V_3 = AV_1$ leads to

$$V_1 = \frac{V_3 + V}{2}. \tag{2.8}$$

In other words, the velocity through the propeller is equal to the average of the velocity upstream and downstream of the propeller. The power expended equals the power imparted onto the fluid, which is equivalent to the change of kinetic energy of the flow as it passes through the propeller. The power added to the fluid is

$$P_{fluid} = \dot{m}\left(\frac{V_3^2 - V^2}{2}\right). \tag{2.9}$$

Conversely, the propulsive power, or rate at which the work is done, is given by the product of thrust and the velocity through the propeller. This can be divided into two parts:

- Useful power: $P_{useful} = TV$;
- Induced power: $P_i = Tw$, w being the propeller induced velocity.

Froude's theorem also states that, for any flow speed, the induced velocity at the outlet of the stream tube by the propeller is twice the velocity induced at the disc,

$$V_3 = V + 2w, \quad V_1 = V + w. \tag{2.10}$$

Concluding, the Actuator Disc Theory does not describe the flow near the disc precisely as the assumptions of a discrete pressure jump and unidirectional flow are not realistic. However, far enough from the disc, such assumptions are reasonable and, for a known thrust and propeller diameter, the induced fluid field becomes more realistic.

2.2 Blade Element Theory

To create an effective propeller and accurately predict its performance, it is crucial to closely examine the blade's geometry and aerodynamics. One way to do this is by using the Blade Element Theory developed by Drzwieck [16, 17] and later enhanced by Prandtl [18]. This theory divides each blade into sections perpendicular to the radial axis, as shown in Figure 2.2. Figure 2.3 provides a visual representation of the blade element and the velocities that affect it. At each section, the flow is analyzed as bidimensional and a force balance is applied to determine the lift, drag, thrust, and torque distributions.

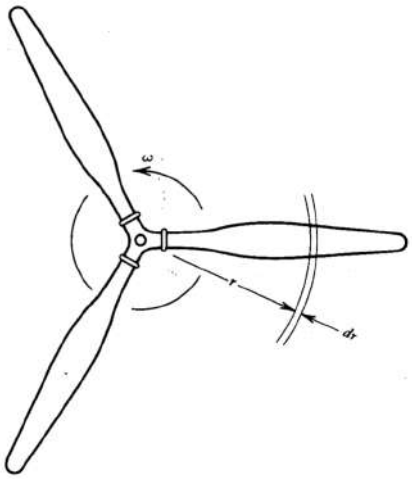

Figure 2.2: Front view of a three-blade propeller rotating with an angular velocity. [15]

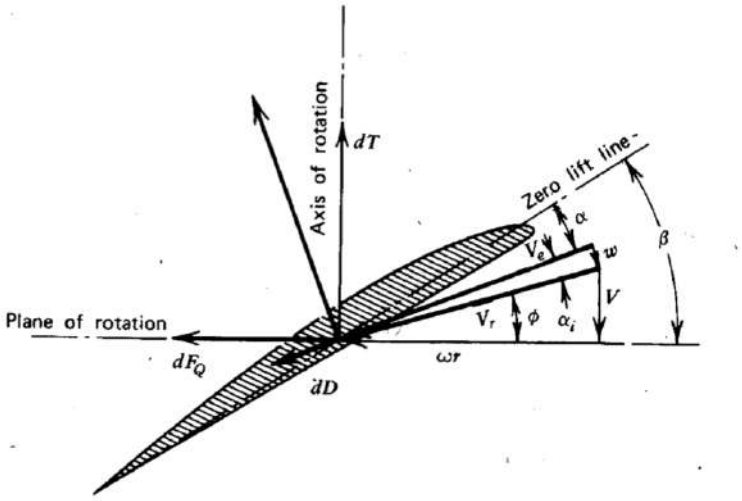

Figure 2.3: Blade element. [15]

Each cross-section experiences a velocity V_R, that results from the vectorial sum of the axial velocity V and the tangential velocity given by ωr. The axial velocity represents the flight velocity, whereas the tangential velocity represents the velocity due to propeller rotation.

The pitch of a propeller corresponds to the distance it would move forward in one revolution as if the propeller screws itself through the air,

$$p = 2\pi r tan(\beta), \tag{2.11}$$

where β is the pitch angle. The angle ϕ is the resultant flow angle relative to the rotation plan, α is the blade element angle of attack and α_i is the induced angle of attack resulting from the induced velocity.

The contribution of each blade element to thrust and torque is given, respectively, by

$$dT = dL\cos(\phi + \alpha_i) - dD\sin(\phi + \alpha_i) \tag{2.12}$$

and

$$dQ = r[dL\sin(\phi+\alpha_i) + dD\cos(\phi+\alpha_i)], \tag{2.13}$$

where dL and dD are the section element lift and drag forces, respectively. From bidimensional aerodynamics,

$$dL = \frac{1}{2}\rho V_E^2 c C_L dr \tag{2.14}$$

and

$$dD = \frac{1}{2}\rho V_E^2 c C_D dr. \tag{2.15}$$

The lift coefficient C_L can be found from

$$C_L = \alpha(\beta - \phi - \alpha_i). \tag{2.16}$$

To determine the contribution of each blade element to the thrust and torque, it is required to know α_i, which depends on the induced velocity w. However, this induced velocity depends on the thrust itself.

In order to get around this problem, we need to assume α_i and the drag-to-lift ratio to be small. Then, according to Figure 2.3, $V_E \simeq V_R$ and the thrust contribution of each section for a propeller with a B number of blades can be written as

$$BdT = \rho(2\pi r dr)(V + V_R\alpha_i\cos\phi)2V_R\alpha_i\cos\phi \quad , \tag{2.17}$$

where it is assumed that $w = V_R\alpha_i$. Another definition comes to the elemental thrust for a propeller with a B number of blades,

$$BdT = BdL\cos\phi = B\frac{1}{2}\rho V_R^2 c C_l dr\cos\phi = B\frac{1}{2}\rho V_R^2 c\alpha(\beta-\phi-\alpha_i)dr\cos\phi. \tag{2.18}$$

Equating the previous two expressions to dT/dr, the induced angle of attack becomes

$$\alpha_i = \frac{1}{2}\left[-\frac{\lambda}{x} - \frac{\sigma\alpha V_R}{8x^2 V_T} + \sqrt{\left(\frac{\lambda}{x} + \frac{\sigma\alpha V_R}{8x^2 V_T}\right)^2 + \frac{\sigma\alpha V_R}{2x^2 V_T}(\beta-\phi)}\right], \tag{2.19}$$

where

$$\lambda = \frac{V}{\omega R} = \frac{V}{V_T} \qquad \sigma = \frac{Bc}{\pi R} \qquad V_R = V_T\sqrt{x^2+\lambda^2}$$

$$\phi = \tan^{-1}(\frac{\lambda}{x}) \qquad V_T = \omega R \qquad x = \frac{r}{R}.$$

Knowing the geometry and rotation and forward speed of the propeller, the induced angle of attack can be determined. It is finally possible to obtain the elemental thrust and torque sections for each cross-section after determining C_L and C_D.

The thrust, power and torque of a propeller are usually expressed in its coefficient form, respectively

$$C_T = \frac{T}{\rho n^2 D^4}, \tag{2.20}$$

$$C_P = \frac{P}{\rho n^3 D^5}, \tag{2.21}$$

and

$$C_Q = \frac{Q}{\rho n^2 D^5} \tag{2.22}$$

where n is the rotational speed in revolutions per second and D is the propeller diameter.

In a dimensionless form, Equations (2.12) and (2.13) can be written as

$$C_T = \frac{\pi}{8}\int_{x_0}^{1}(J^2+\pi^2x^2)\frac{Bc}{\pi R}[C_l\cos(\phi+\alpha_i) - C_d\sin(\phi+\alpha_i)]\,dx, \tag{2.23}$$

$$C_P = \frac{\pi}{8}\int_{x_0}^{1}\pi x(J^2+\pi^2x^2)\frac{Bc}{\pi R}[C_l\cos(\phi+\alpha_i) + C_d\sin(\phi+\alpha_i)]\,dx\ , \tag{2.24}$$

where r_0 is the hub station where the blade begins and J is a quantity called advance ratio and is defined by

$$J = \frac{V}{nD}. \tag{2.25}$$

Finally, it is possible to calculate the propeller efficiency given by

$$\eta = \frac{C_T J}{C_P}. \tag{2.26}$$

2.3 Reynolds-Averaged Navier-Stokes Model

The first problems handled by CFD were relatively straightforward, 2D, incompressible, steady-state situations that usually were limited to laminar flows. It was not until 1967 that the first 3D CFD simulation was completed [19]. Over the years, progress has become much faster as both computational power and modeling approaches advanced.

For compressible Newtonian fluids, the Navier-Stokes equations are formulated as

$$\frac{\partial\rho}{\partial t} + \frac{\partial}{\partial x_i}(\rho v_i) = 0 \tag{2.27}$$

$$\frac{\partial}{\partial t}(\rho v_i) + \frac{\partial}{\partial x_j}(\rho v_j v_i) = -\frac{\partial p}{\partial x_i} + \frac{\partial \tau_{ij}}{\partial x_j} \tag{2.28}$$

$$\frac{\partial}{\partial t}(\rho E) + \frac{\partial}{\partial x_j}(\rho v_j H) = \frac{\partial}{\partial x_j}(v_i\tau_{ij}) + \frac{\partial}{\partial x_j}\left(k\frac{\partial T}{\partial x_j}\right), \tag{2.29}$$

where v_i denotes a velocity component $\vec{v} = [v_1, v_2, v_3]^T$ and x_i is a coordinate direction. The components

of the viscous stress tensor τ_{ij} are defined as

$$\tau_{ij} = 2\mu S_{ij} + \lambda \frac{\partial v_k}{\partial x_k}\delta_{ij} = 2\mu S_{ij} - \left(\frac{2\mu}{3}\right)\frac{\partial v_k}{\partial x_k}\delta_{ij}. \tag{2.30}$$

The variable λ represents a viscosity coefficient and the strain-rate sensor is defined by

$$S_{ij} = \frac{1}{2}\left(\frac{\partial v_i}{\partial x_j} + \frac{\partial v_j}{\partial x_i}\right). \tag{2.31}$$

The total energy E and the total enthalpy H are, respectively,

$$E = e + \frac{1}{2}v_i v_i \quad \text{and} \quad H = h + \frac{1}{2}v_i v_i. \tag{2.32}$$

A key development was the incorporation of turbulence modeling into the CFD solutions. The concept of ”eddy viscosity” was introduced in the first approaches and it reflects an apparent increase in viscosity caused by small-scale chaotic fluid motions. CFD simulations do not attempt to actually capture such motions, rather they simulate their effect by an increase in the fluid viscosity.

Figure 2.4 displays different turbulence models sorted according to their decreasing level of complexity.

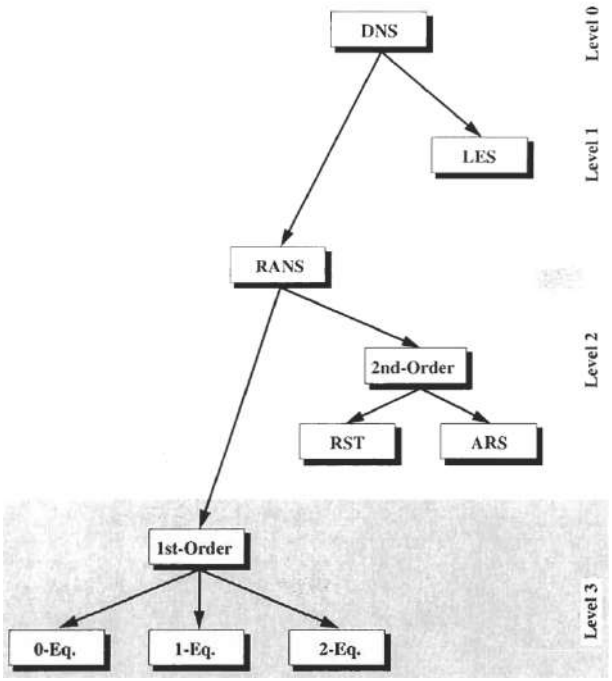

Figure 2.4: Hierarchy of turbulence models. DNS: Direct Numerical Simulation; LES: Large-Eddy Simulation; RANS: Reynolds-Averaged Navier-Stokes equations; RST: Reynolds-Stress Transport models; ARS: Algebraic Reynolds-Stress models; 0-, 1-, 2- Eq.: Algebraic, one-, two-equations models. [20]

It is important to understand that there is no single turbulence model which can predict accurately all kinds of turbulent flows. Each model has its advantages and weaknesses. Hence, it is important to

always ask whether the model includes all the significant features of the flow being investigated. In this study, RANS-based turbulence models were utilized to investigate the fluid properties around a rotating propeller.

Additionally, when selecting a turbulence model, it is vital to consider the computational effort required versus the accuracy needed for the specific application. In numerous instances, a less complex turbulence model can predict some overall measures with the same precision as a more intricate model.

The Reynolds-Averaging methodology involves breaking down flow variables into mean and fluctuating components. This means that the Navier-Stokes equations are solved for their mean values. In the case of incompressible flows, the velocity and pressure variables in these equations are defined as follows:

$$v_i = \bar{v_i} + v_i' \qquad p_i = \bar{p_i} + p_i' \tag{2.33}$$

where the mean value is denoted by an overbar and the turbulent fluctuations by a prime. The mean values are obtained by an averaging procedure. Three different forms of Reynolds averaging are:

- *Time averaging*: the mean value does not vary in time.

$$\bar{v_i} = \lim_{T\to\infty} \frac{1}{T} \int_t^{t+T} v_i \, dt \tag{2.34}$$

- *Spatial averaging*: the mean value is uniform in space.

$$\bar{v_i} = \lim_{\Omega\to\infty} \frac{1}{\Omega} \int_\Omega v_i \, d\Omega \tag{2.35}$$

- *Ensemble averaging*: the mean value $\bar{v_i}$ remains a function of time and space.

$$\bar{v_i} = \lim_{N\to\infty} \frac{1}{N} \sum_{m=1}^{N} v_i \tag{2.36}$$

Applying either time or ensemble averaging, the incompressible Navier-Stokes equations (continuity and momentum) are called the Reynolds-Averaged Navier-Stokes equations (RANS):

$$\frac{\partial \bar{v_i}}{\partial x_i} = 0 \tag{2.37}$$

$$\rho \frac{\partial \bar{v_i}}{\partial t} + \rho \bar{v_j} \frac{\partial \bar{v_i}}{\partial x_j} = -\frac{\partial \bar{p}}{\partial x_i} + \frac{\partial}{\partial x_j} \left(\overline{\tau_{ij}} - \rho \overline{v_i' v_j'} \right). \tag{2.38}$$

$\tau_{ij}^R = -\rho \overline{v_i' v_j'}$ is the Reynolds-stress tensor and it represents the transfer of momentum due to turbulent fluctuations. This tensor is unknown and needs to be modeled. There are three approaches [21]:

- Eddy Viscosity hypothesis;
- Non-linear Eddy Viscosity;
- Reynolds-Stress Transport equations.

The first two approaches attempt to predict the turbulent viscosity, whether the last one uses transport equations for the Reynolds stresses. The last method is suitable for complex 3D turbulent flows but the computational cost increases appreciably. The most widely used approaches for eddy viscosity involve three main model families [21, 22]:

- Spalart-Allmaras (1 equation): employs transport equation for an eddy viscosity variable;
- k-ϵ (2 equations): it is based on the solution of equations for the turbulent kinetic energy and the turbulent dissipation rate;
- k-ω (2 equations): it is based on the solution of equations for the turbulent kinetic energy and the specific dissipation rate.

The k-ϵ model is employed in the wake region of the boundary layer, while the k-ω approach is employed in the sub-layer of the boundary layer. On one hand, the k-ω provides higher numerical stability. However, it is strongly sensitive to the free stream value of ω. Furthermore, the k-ω method is also used in the logarithmic part of the boundary layer, providing higher accuracy than the k-ϵ approach in adverse pressure flows and compressible flows.

There is a variant of the last model called the k-ω Shear Stress Transport (SST) that merges the k-ω model with a high Reynolds number k-ϵ model in order to combine the positive features of both. One distinct feature of the SST model is the modified eddy-viscosity function in order to improve the accuracy of prediction of flows with strong adverse pressure gradients and of pressure-induced boundary layer separation. This turbulence model was used in previous studies such as [14, 23–25]. These different models will be applied in the next chapters and comparisons on the propeller performance predictions will be made.

2.4 Spatial Discretization and Mesh Selection

The discretization of the physical domain is a process called meshing that results in a grid on which the conservation equations are solved. This process requires the division of the domain of interest into discrete non-overlapping cells. These grids are classified according to a wide range of characteristics: structure, orthogonality or cell shape.

In structured grids, as shown in Figure 2.5, each grid point is identified by the indices i, j and k. These indices represent a linear address space in the computer memory. This property allows access to the neighbor cells in a simple way, representing an advantage of such structures. However, it is pretty challenging to generate structured grids for complex geometries. The grid cells are quadrilaterals in 2D and hexahedrons in 3D.

In unstructured grids, cells have no particular ordering and can be triangles or quadrilaterals in 2D and hexahedrons, tetrahedrons, prisms, or pyramids in 3D, as shown in Figure 2.6. Unstructured meshes offer the most significant flexibility in the treatment of complex geometries.

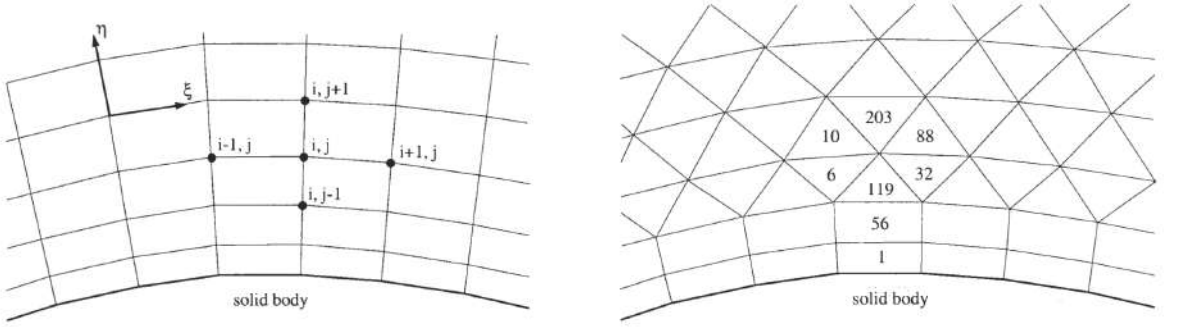

(a) Structured 2D mesh. [20] (b) Unstructured 2D mesh. Numbers mark individual cells.[20]

Figure 2.5: Classification of a mesh according to its structure.

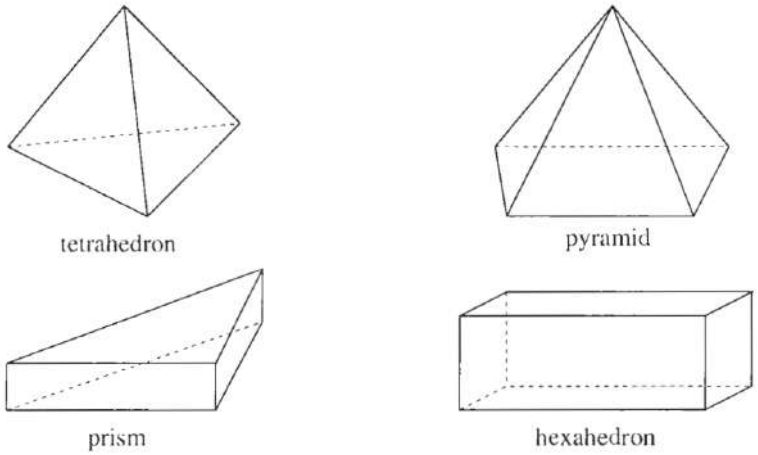

Figure 2.6: Type of elements used for generation of 3D meshes.[20]

The mesh elements are entirely bounded by faces that are shared with neighbor cells except at the boundaries. The grid should also be smooth, i.e., there should not be significant differences in the volumes or in the aspect ratio of adjacent elements. Otherwise, the numerical errors can increase and the solution will lack accuracy completely.

Once the grid is generated, the question that follows is how to discretize the governing equations. The numerical solution of the governing partial differential equations consists of finding the values of an arbitrary flow property ϕ at the grid elements or nodes resulting from the meshing process. The distribution of ϕ is discretized, i.e., the governing equations are converted into a set of algebraic equations for the discrete values of ϕ. There are different methods that can be employed in order to obtain this conversion [26]:

- Finite differences;
- Finite volumes;
- Finite elements.

In all techniques, the primary objective is to replace the continuous exact solution of the governing

partial differential equations with discrete values. The discrete values of ϕ are usually obtained by resolving a series of algebraic equations that relate the values of neighboring grid elements to one another. There are various methods to solve these algebraic equations in order to obtain such discrete values, which can be classified into two categories:

- Direct Methods (the solution is obtained using a relatively complex algorithm once);
- Iterative Methods (they follow a guess-and-correct procedure to refine the estimated solution by repeatedly solving the discrete system of equations).

The present study concentrates exclusively on the Finite Volume method. The discretization process used in the Finite Volume Method involves two steps. In the first step, the governing equations are integrated over the grid elements and transformed into balance equations over each element. The result is a set of semi-discretized equations.

The conservation equation for an arbitrary flow variable ϕ is given by

$$\underbrace{\frac{\partial(\rho\phi)}{\partial t}}_{\text{transient term}} + \underbrace{\nabla\cdot(\rho v\phi)}_{\text{convective term}} = \underbrace{\nabla\cdot(\Gamma^{\phi}\nabla\phi)}_{\text{diffusion term}} + \underbrace{Q^{\phi}}_{\text{source term}} . \tag{2.39}$$

Integrating over the volume of element C (as shown in Figure 2.7) for steady-state conditions,

$$\int_{V_C} \nabla\cdot(\rho v\phi)\,dV = \int_{V_C} \nabla\cdot(\Gamma^{\phi}\nabla\phi)\,dV + \int_{V_C} Q^{\phi}\,dV. \tag{2.40}$$

The divergence theorem is applied to the volume integrals of diffusion and convection terms and the semi-discrete steady-state equation for an element E is simplified to

$$\sum(\rho v\phi - \Gamma^{\phi}\nabla\phi)_f \cdot S_f = Q_C^{\phi}V_C. \tag{2.41}$$

The second step of the Finite Volume Method transforms Equation (2.41) into an algebraic equation by expressing the face and volume fluxes in terms of the values of the arbitrary property ϕ at the neighbor cell centers (Figure 2.7). This process occurs through flux linearization. The total flux is given by the sum of the convection and diffusion fluxes,

$$J^{\phi} = J^{\phi,C} + J^{\phi,D} = \rho v\phi - \Gamma^{\phi}\nabla\phi. \tag{2.42}$$

The total flux for a specific face f can be written as

$$J_f^{\phi}\cdot S_f = FluxC_f\phi_C + Fluxf_f\phi_f + FluxV_f, \tag{2.43}$$

where the first two terms represent the contributions of the two elements sharing the face f, whereas the last term describes the non-linear contribution.

Finally, Equation (2.41) can be written as

$$\sum_{f\sim nb(C)} (J_f^{\phi} \cdot S_f) = \sum_{f\sim nb(C)} (FluxC_f\phi_C + FluxF_f\phi_f + FluxV_f) = Q_C^{\phi}V_C, \tag{2.44}$$

where $nb(C)$ relates to all the faces shared by element C with its neighbor cells.

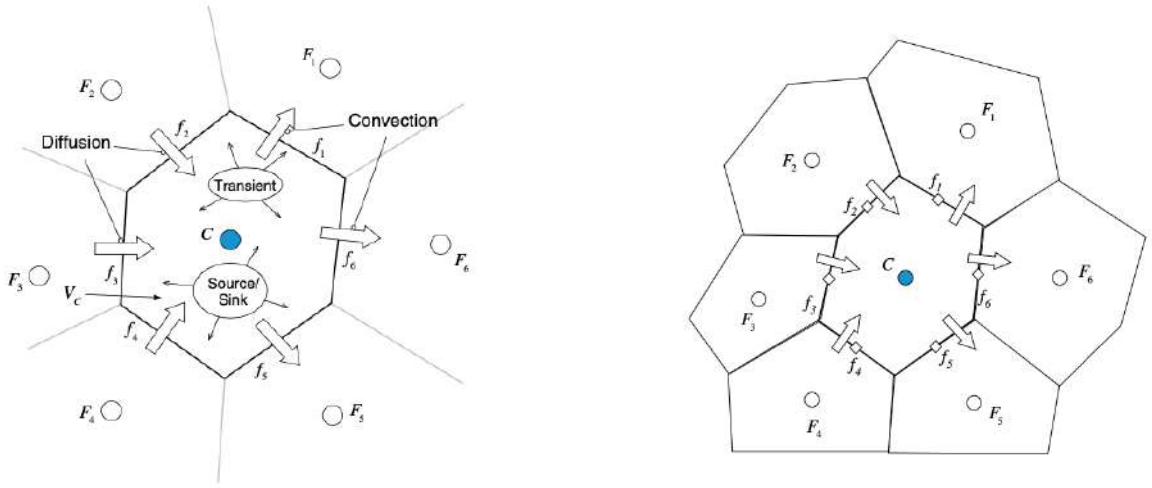

(a) Conservation in a grid element C. [26]

(b) Fluxes at element surfaces.[26]

Figure 2.7: Finite volume method.

2.4.1 Solvers Selection

ANSYS® Fluent® allows the user to choose one of the two numerical methods [27]:

- pressure-based solver;
- density-based solver.

In both methods, the velocity field is derived from the momentum equations. The density-based method utilizes the continuity equation to obtain the density field, while the pressure field is determined by applying the equation of state. In contrast, the pressure-based method involves solving a pressure or pressure correction equation, obtained by manipulating the continuity and momentum equations, to extract the pressure field.

For the analysis of the propellers, the pressure-based solver was employed to predict their performance in this study. Furthermore, two pressure-based solver algorithms are available in ANSYS® Fluent®. A segregated algorithm, and a coupled algorithm. In this study, a segregated algorithm (SIMPLE) was chosen and Figure 2.8 presents an overview of it.

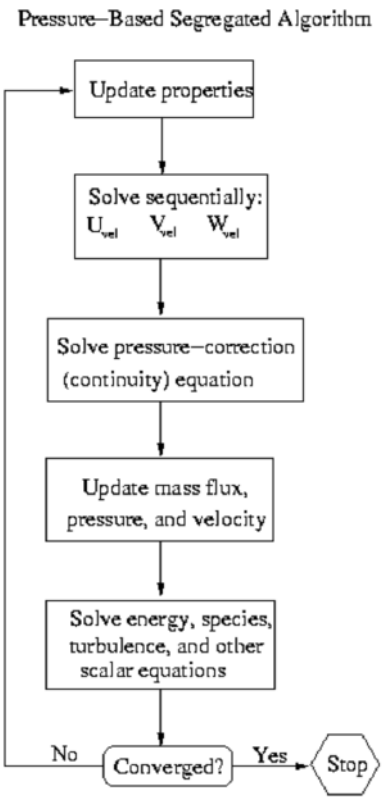

Figure 2.8: Pressure-based segregated algorithm. [27]

2.4.2 Steady vs Unsteady Approaches

The case study of rotating propellers is a clear example of constant rigid body motion that can be solved using steady-state approaches even though the flow field is clearly unsteady. These approaches involve the use of moving frames of reference that may translate or/and rotate. These approaches are useful when the transient effects are not that important compared with the average values. ANSYS® Fluent® provides two different methods for steady-state approaches [27]:

- Multiple Reference Frame model (MRF);
- Mixing Plane Model (MPM).

It is important to point out that both approaches (MRF and MPM) consist of static meshes and that both try to solve an unsteady problem with a steady-state approach. The difference between both regards the treatment of the interfaces between static and moving cell zones. In this study, the MRF model was used.

The MRF model is the more straightforward of the two methods to apply to multiple zones. It involves a steady-state approximation that allows for rotational and/or translational speeds to be assigned to individual cell zones. The flow in each moving cell zone is solved using the moving reference frame equations.

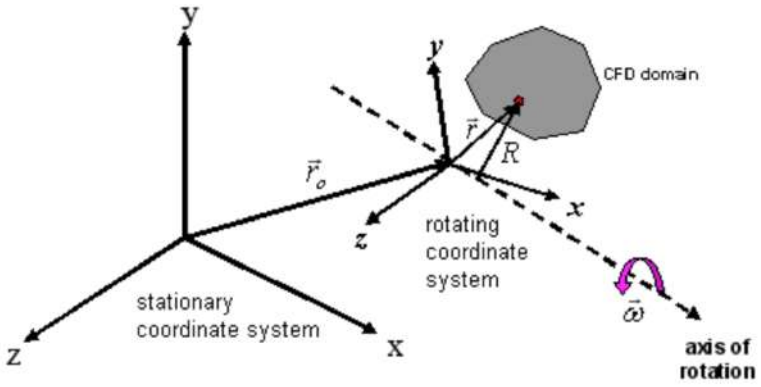

Figure 2.9: Stationary and rotating reference frames. [27]

According to Figure 2.9, the fluid velocities can be transformed from the stationary frame to the rotating frame using the following

$$\vec{v_r} = \vec{v} - \vec{u_r}, \tag{2.45}$$

where $\vec{u_r} = \vec{\omega} \times \vec{r}$. $\vec{v_r}$ is the relative velocity (the velocity viewed from the rotating frame), $\vec{v}$ is the absolute velocity (the velocity viewed from the stationary frame), and $\vec{u_r}$ is the "whirl" velocity (the velocity due to the moving frame).

When the equations of motion are solved in the rotating reference frame, the acceleration of the fluid is augmented by additional terms that appear in the momentum equation.

The Navier-Stokes equations for a steadily rotating plane can then be written as

$$\frac{\partial \rho}{\partial t} + \nabla \cdot \rho \vec{v_r} = 0 \tag{2.46}$$

$$\frac{\partial}{\partial t}\rho\vec{v} + \nabla \cdot (\rho \vec{v_r}\vec{v}) + \rho(\vec{\omega} \times \vec{v}) = -\nabla p + \nabla \cdot \tau + \vec{F} \tag{2.47}$$

$$\frac{\partial}{\partial t}\rho\vec{E} + \nabla \cdot (\rho \vec{v_r} H + p\vec{u_r}) = \nabla \cdot (k\nabla T + \tau \cdot \vec{v}) + S_h. \tag{2.48}$$

If the zone is stationary ($\omega = 0$), the equations reduce to their stationary forms. At the interfaces between cell zones, a local reference frame transformation is performed to enable flow variables in one zone to be used to calculate fluxes at the boundary of the adjacent zone.

Unsteady approaches involve mesh motion. The simplest way of defining grid movement is the Rigid Body Motion Method which can be applied to the study of rotating propellers. However, unsteady approaches are very demanding computationally but if transient simulations are needed, then this is the only possible way. Rigid Body Motion implies that both the solid body and the whole mesh are not deformed. Also, the mesh moves according to an imposed motion (rotationally and/or translationally). The Navier-Stokes equations are solved for the moving mesh in a standard way and if the simulations are run with a sufficiently small time step, the solution strategy is able to capture the unsteady flow motion. Unsteady approaches are much more time-consuming. In later chapters, both steady and unsteady

approaches will be conducted.

2.4.3 Boundary Layer

Turbulent flows are substantially affected by the presence of walls. When the turbulence equations are solved near the wall, the wall effects need to be modeled. The mean velocity field is affected due to the no-slip condition satisfied at the wall. Furthermore, very close to the wall, the kinematic blocking reduces normal fluctuations and viscous damping reduces the tangential velocity fluctuations. It is close to the wall that the solution variables have large gradients, such as pressure and velocity in the case of rotating propellers.

The modeling of flow near the wall greatly affects the accuracy of numerical solutions. The success of predicting wall-bounded turbulent flows largely depends on how well the flow near the wall is represented. To obtain precise results for the boundary layer, it is crucial to ensure that the overall resolution of the layer is adequate. When working with unstructured meshes, it is advisable to create prism layers near the wall, comprising 20 or more layers [27]. It is important to note that the thickness of the prism layer should be greater than that of the boundary layer.

The wall effects are modeled by separating them into three layers, laminar or viscous sublayer, buffer layer and fully turbulent layer ([27]), as shown in Figure 2.10.

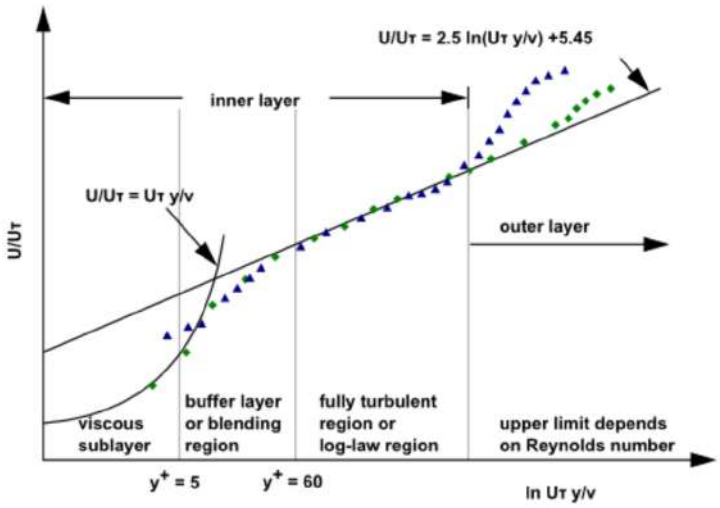

Figure 2.10: Subdivisions of the near-wall region. [27]

The $y+$ parameter is the non-dimensional height of the first layer of the boundary layer, defined as

$$y+ = \frac{yu_\tau}{\nu} \ , \tag{2.49}$$

where u_τ is the friction velocity, y is the absolute height of the first layer and ν is the kinematic viscosity.

Wall functions are a set of semi-empirical formulas and functions and are used to link the solution variables at the near-wall mesh cells and the corresponding quantities on the wall. The wall functions embrace both the law of the wall for the mean velocity and temperature and the formulas of near-wall

turbulent flow properties. The law-of-the-wall for mean velocity is given by

$$U^* = \frac{1}{k} ln(Ey*). \tag{2.50}$$

U^* is the dimensionless velocity which can also be defined as

$$U^* = \frac{\rho U u_\tau}{\tau_w} \ , \tag{2.51}$$

where y^* is the dimensionless distance from the wall.

Depending on the turbulence model chosen, ANSYS® Fluent® offers different wall-function approaches [27]:

- Standard wall functions;
- Scalable wall functions;
- Non-equilibrium wall functions;
- Enhanced Wall Treatment;
- User-defined wall functions.

The three first approaches' results deteriorate under refinement of the prism layer. For values of $y+ < 15$, the wall functions will deteriorate and the accuracy of the solutions will decrease.

To address this issue, the Enhanced Wall Treatment was developed. This approach employs advanced formulations that enable consistent mesh refinement without compromising the accuracy of the results. It is compatible with both turbulence models analyzed in our study, namely $k - \epsilon$ and $k - \omega$.

For the $k - \epsilon$ model to work effectively with the Enhanced Wall Treatment, the near-wall mesh must be fine enough to resolve the viscous sublayer, i.e., when $y+ < 1$. On the other hand, the $k - \omega$ model is not dependent on the height of the first layer.

Chapter 3

CFD Modelling

This Chapter will delve into the primary analysis of two rotating commercial propellers. The focus will be on high-fidelity numerical analyses and it will be presented in three stages: creating the CAD geometry of the propeller under examination, modelling the flow around it, and constructing the mesh.

3.1 Problem Description and Studied Propellers

Before conducting a high-fidelity numerical analysis of the flow around a rotating propeller, three stages must be completed, as illustrated in Figure 3.1.

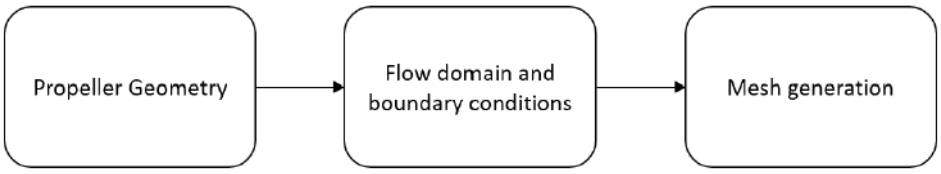

Figure 3.1: CFD pre-processing steps.

To analyze the propeller's performance, the initial stage involves constructing a CAD geometry. Next, a model is built to simulate the flow around the propeller and assign the necessary boundary conditions. The final step involves generating the mesh of the model in ANSYS® Meshing™, followed by imposing various flow conditions in ANSYS® Fluent®.

Whether a low or high-fidelity numerical analysis is conducted, the results obtained need to be validated with experimental testing. Due to the lack of equipment, it was not possible to conduct the experimental testing for dynamic conditions. To overcome this problem, the propellers studied are commercial propellers whose experimental data is available online. Hence, two APC propellers were selected. The first propeller analyzed was the APC 14"x13" Sport [28], which means that the propeller has a diameter equal to 14 inches and a pitch of 13 inches. The second propeller chosen was the APC 10"x8" Sport [29]. A different pitch and diameter were selected in order to analyze its impact on the propeller performance. The experimental results were obtained from [7].

3.2 Propeller Geometry

When conducting CFD simulations for commercial small-scale propellers, ensuring that the CAD model used accurately represents the real model can be a challenge. The manufacturing process may not always be precise due to the propeller's small thickness and chord dimensions. Even slight deviations in pitch distributions resulting from manufacturing can significantly impact propeller performance. This issue can be exacerbated if manufacturers do not provide detailed geometry information. To mitigate this problem, APC propellers were selected as the manufacturer provides comprehensive blade geometry details, including airfoil information for each propeller [30].

In order to build a good representation of the APC 14"x13" Sport and APC 10"x8" Sport propellers, the procedure illustrated in Figure 3.2 was followed.

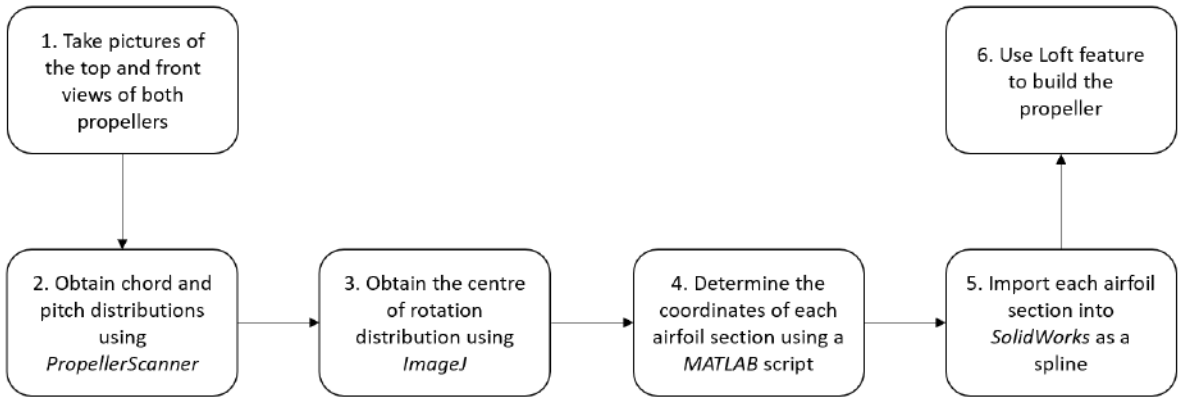

Figure 3.2: Geometry procedure.

1. Pictures of the top and front views of the propeller in the study were taken. Both images should be aligned horizontally and have equal diameters.

Figure 3.3: Front view of APC 10"x8" Sport. Source: [7]

Figure 3.4: Top view of APC 10"x8" Sport. Source: [7]

2. The chord and twist distributions along the blades' radius were obtained from PropellerScanner, a software developed by Martin Hepperly [31]. This program attempts to reconstruct the blade

shape of a two-bladed propeller and it uses a side view and a front view as input to trace the blade shape. Both blades are taken into account and the average of both sides is presented as the nominal propeller geometry. Several studies have evaluated the accuracy of this software, including Daniel Uhlig's research [32] that compared the values of chord and pitch distributions after slicing a propeller. The results were highly satisfactory, with the chord distributions in agreement and the pitch distributions having only errors between 1° and 2°. PropellerScanner software provides a quick estimate of propeller geometry. The main window of this program is presented in Figure 3.5.

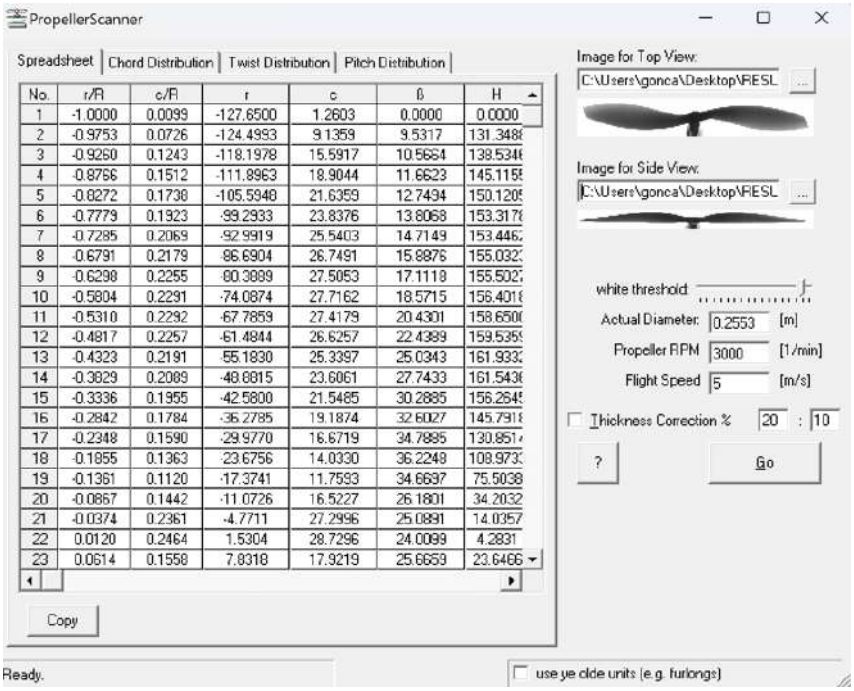

Figure 3.5: Main window of PropellerScanner.

The chord and beta distribution obtained from PropellerScanner for the APC 14" $\times$ 13" Sport and APC 10" $\times$ 8" Sport propellers are in Appendices A and B, respectively.

3. To ensure precise reproduction of the leading and trailing edges, it is essential to determine the distribution of the centers of rotation (the line where the airfoils are centered) alongside the accurate results of the chord and pitch distributions provided by PropellerScanner. The image-processing software ImageJ [33] was used to obtain this information.

(a) Front view allow. (b) Fluxes at element surfaces.

Figure 3.6: ImageJ processing tool.

This software is capable of detecting edges and accurately identifying pixel intensity, as demonstrated in Figure 3.6. Through precise image scaling, it is possible to determine the coordinates of

both leading and trailing edges. To estimate the center of rotation of each airfoil, knowledge of the airfoil type used in each blade is necessary. To streamline the analysis process, it was chosen to examine propellers that have distributions of Clark-Y airfoils. Hence, it is assumed that the center of rotation is located at 25% of the chord. The coordinates of the axis of rotation for the APC 14" $\times$ 13" Sport and APC 10" $\times$ 8" Sport propellers can be located in Appendices A and B, respectively.

4. By using Matlab®, the scripts available in Appendix C were used to determine the coordinates of every airfoil along the radius with the inputs obtained from steps 2 and 3. The Clark-Y airfoil coordinates from [34] were considered in the script, and chord transformations and rotations around the center of rotation were performed.

5. In SolidWorks®, every airfoil section was imported as a separate spline (Figure 3.7).

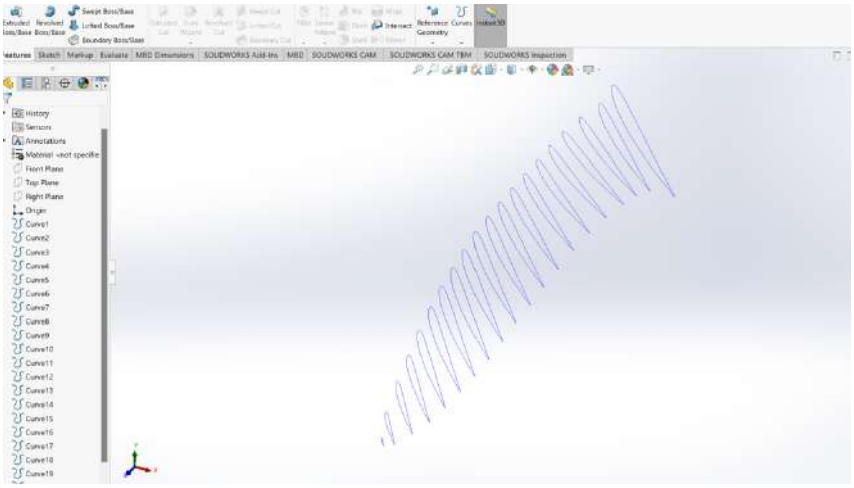

Figure 3.7: Each airfoil is imported to SolidWorks®.

6. By using the Loft feature and having access to the hub diameter provided by APC, it was possible to create a precise depiction of the actual propeller, as demonstrated in Figure 3.8.

Figure 3.8: Loft feature and final design in SolidWorks®.

The final geometries of the propellers are shown in Figures 3.9 and 3.10. To conclude, based on the limited information available on the propeller geometry, it can be said that the CAD models of the two

propellers analyzed are a suitable representation of the original propeller.

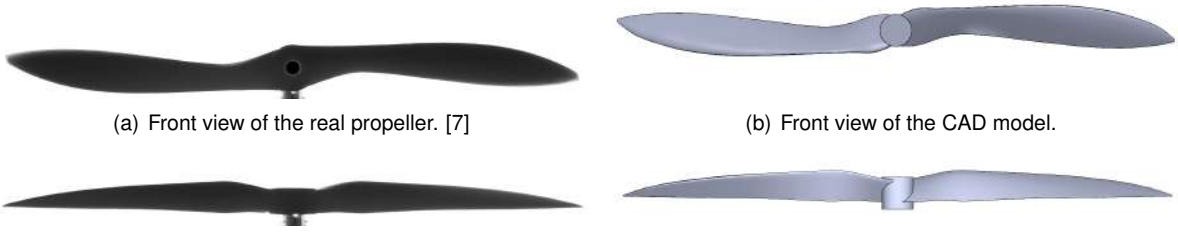

(a) Front view of the real propeller. [7]

(b) Front view of the CAD model.

(c) Top view of the real propeller. [7]

(d) Top view of the CAD model.

Figure 3.9: Real vs CAD model APC 14”x13” Sport.

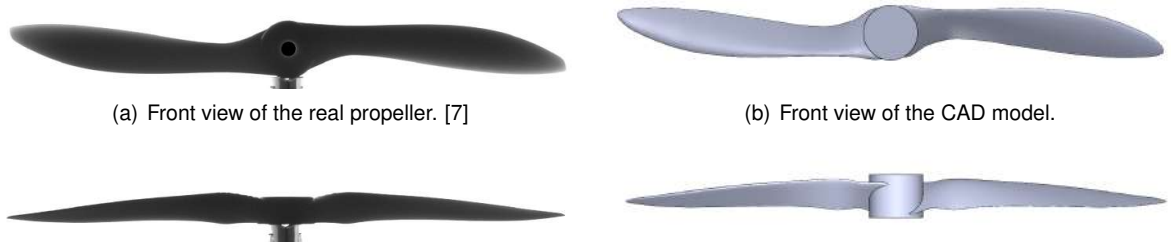

(a) Front view of the real propeller. [7]

(b) Front view of the CAD model.

(c) Top view of the real propeller. [7]

(d) Top view of the CAD model.

Figure 3.10: Real vs CAD model APC 10”x8” Sport.

3.3 Flow Domain and Boundary Conditions

The second pre-processing stage deals with setting up the CFD environment for analyzing the propeller. The flow domain comprises two regions - a stationary one that will be solved in a steady reference plane and a rotating one that encloses the propeller and will be solved on a rotating reference frame moving with it. A sliding interface connects these two regions. The choice of geometric boundary for both fluid regions is consistent with previous studies ([14, 25, 35]).

Figure 3.11 shows that the stationary domain’s height and length are eight times the propeller’s diameter. Meanwhile, the cylinder diameter of the rotating region is 0,4D, and its height is 1,1D. These dimensions were utilized by various authors in previous studies, such as [14]. Accurate dimensions for the rotating region are crucial in obtaining physically accurate results. Thus, a sensitivity analysis of the rotating region’s dimensions will be conducted later on. Moreover, the boundaries of the stationary fluid region should be set far enough from the propeller so that the flow around it is not affected.

The APC 14”x13” Sport and APC 10”x8” Sport propellers are designed with two blades, enabling rotational periodicity. As illustrated in Figure 3.13, only half of the flow domain is calculated, resulting in a decrease in the number of cells and computational cost.

After building the fluid domain, another critical step before starting to simulate is the assignment of the boundary conditions. Two types of conditions are simulated: hovering flight and vertical climb flight. In hovering flight tests, the free stream velocity is set to zero, only the propeller has a rotational speed.

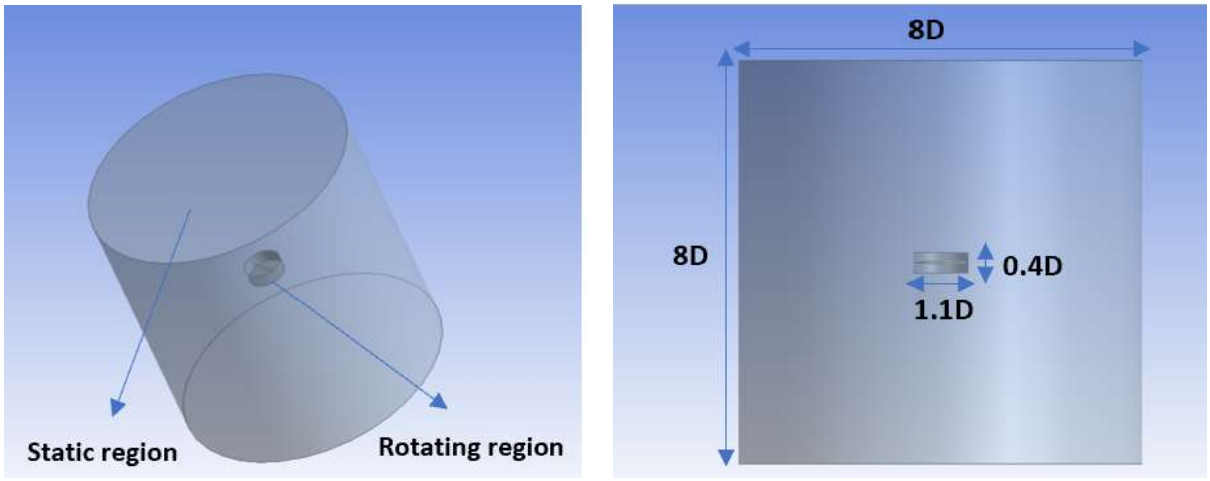

(a) Different fluid regions.

(b) Dimensions of the fluid regions.

Figure 3.11: Flow domain around the rotating propeller.

In vertical flight climb tests, both the rotational speed of the propeller and free stream velocity are set.

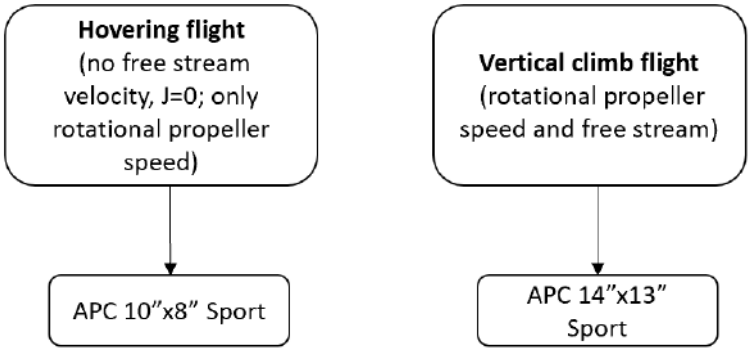

Figure 3.12: Types of flow conditions simulated.

As shown in Figure 3.12, hovering flight simulations were realized on the APC 10”x8” Sport, while vertical climb flight simulations were realized on the APC 14”x13” Sport.

Hence, boundary conditions can be assigned according to each type of simulation conducted. The boundary conditions used in the CFD simulations are presented in Table 3.1 and Table 3.2 for the vertical climb and hovering flight configurations, respectively.

Table 3.1: Boundary conditions for vertical climb flight simulations.

Boundary	Boundary condition	Turbulence boundary condition
Inlet	Velocity-inlet $V = V_{freestream}$	0.1% Turbulence intensity
Outlet	Pressure-outlet $p = p_{atm}$	0.1% Turbulence intensity
Propeller	No-slip wall	-
Periodic outer walls	No-slip wall	-

The inlet boundary condition describes the entrance of the flow and it varies according to the flight configuration. The outflow boundary condition defines the exit of the flow and pressure was set to

Table 3.2: Boundary conditions for hovering flight simulations.

Boundary	Boundary condition	Turbulence boundary condition
Inlet	Pressure-inlet $p = p_{atm}$	0.1% Turbulence intensity
Outlet	Pressure-outlet $p = p_{atm}$	0.1% Turbulence intensity
Propeller	No-slip wall	-
Periodic outer walls	No-slip wall	-

atmospheric. The no-slip condition was set to every wall of the domain, including the propeller and outer walls of the stationary fluid region. The turbulence intensity was chosen according to the wind tunnel measurements made in [6].

Finally, a scheme of the boundary conditions assigned to the fluid domain is presented in Figure 3.13.

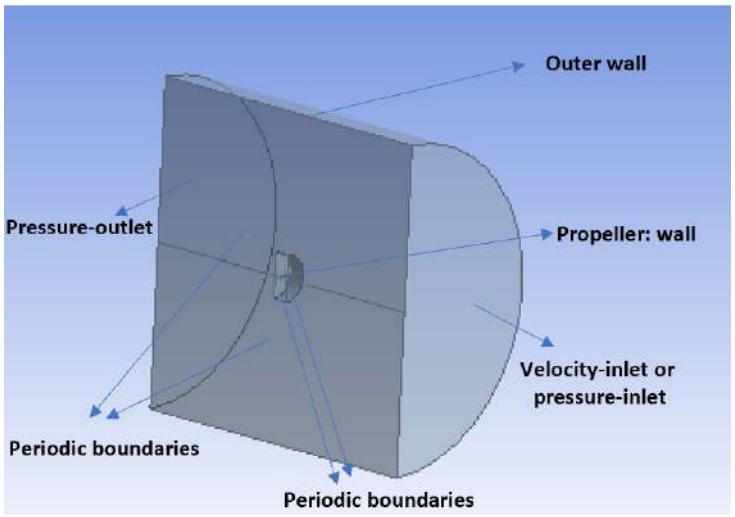

Figure 3.13: Boundary conditions when the free stream direction is from right to left.

3.4 Mesh Generation

In order to effectively simulate and predict performance, it is imperative to acquire a mesh of the domain that meets high standards of quality. This will yield dependable results that closely resemble those generated by experimental testing within a wind tunnel. The quality of the mesh is a determining factor in the rate of convergence, simulation duration, and overall performance.

ANSYS® Meshing™ was used to generate the mesh. For the present investigation, a non-structured mesh comprising tetrahedral elements (as depicted in Figure 2.6) was opted for both the stationary and rotating fluid domains. Prism elements were used for crafting the boundary layer encircling the propeller walls. By leveraging an unstructured mesh, the complex geometry mandated minimal intervention from the user. The mesh sizing parameters for both propellers are presented in Table 3.3. However, the most important parameter is not tabulated, the Element Size. A sensitivity analysis of this parameter will be done in the next Chapter.

Table 3.3: Mesh sizing parameters.

Physics preference	CFD
Solver preference	Fluent
Element order	Linear
Growth rate	1.2
Mesh defeaturing	Yes
Capture curvature	Yes
Curvature normal angle	34°
Capture proximity	Yes
Proximity gap factor	1
Proximity size sources	Faces and Edges
Triangle surface mesher	Program controlled

Figures 3.14 and 3.15 provide a closer view of the unstructured mesh generated in both fluid regions. It is noteworthy that each region was subjected to different body sizing. Particular attention was given to the rotating domain, where the cells were made smaller along the propeller.

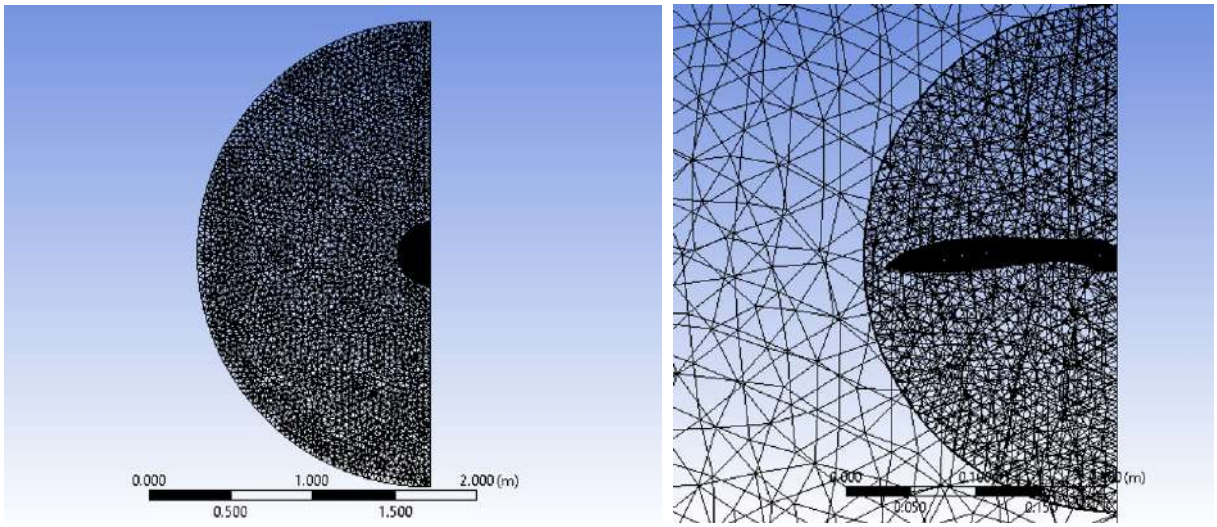

Figure 3.14: Mesh generation.

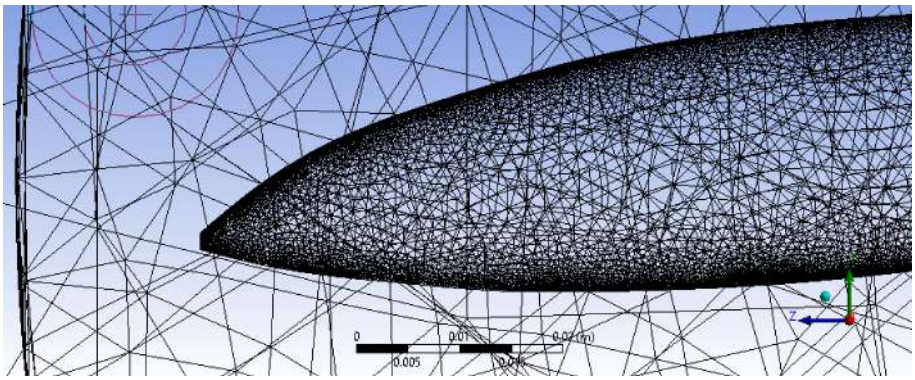

Figure 3.15: Mesh generation on the rotating region.

As seen in Section 2.4.3, to ensure accurate outcomes in viscous flow simulations, it is critical to appropriately address the boundary layer. Neglecting this aspect leads to a deficient representation of the viscous sublayer, resulting in inaccurate results. Thus, constructing a well-organized boundary layer mesh is essential for achieving the desired level of accuracy.

For the boundary layer enveloping the propeller walls, prism elements were employed. ANSYS® Meshing™'s prescribed settings for this purpose are listed in Table 3.4.

Table 3.4: Boundary layer parameters.

Inflation Option	Smooth Transition
Transition Ratio	0.272
Number of Layers	24
Growth Rate	1.2
Inflation Algorithm	Pre
Collision Avoidance	Layer Compression
Gap Factor	0.5
Growth Rate Type	Geometric
Maximum Angle	140°
Fillet Ratio	1
Use Post Smoothing	No

The determination of the number of layers was based on the non-dimensional height of the initial boundary layer, which is represented by the parameter $y+$ calculated using Equation (2.49).

The ANSYS® Fluent® User's Guide [27] provides guidance on parameter settings to achieve accurate results. When utilizing the $k-\epsilon$ turbulence model with Enhanced Wall Treatment in Fluent simulations, it is recommended to maintain a value below 1 for optimal performance. In contrast, the $k-\omega$ turbulence model remains unaffected by the height of the first layer. Nevertheless, it is crucial to verify that the maximum value of this parameter along the propeller blade remains below 1 after each simulation. Figure 3.16 shows the boundary layer mesh at 75% of the blade radius.

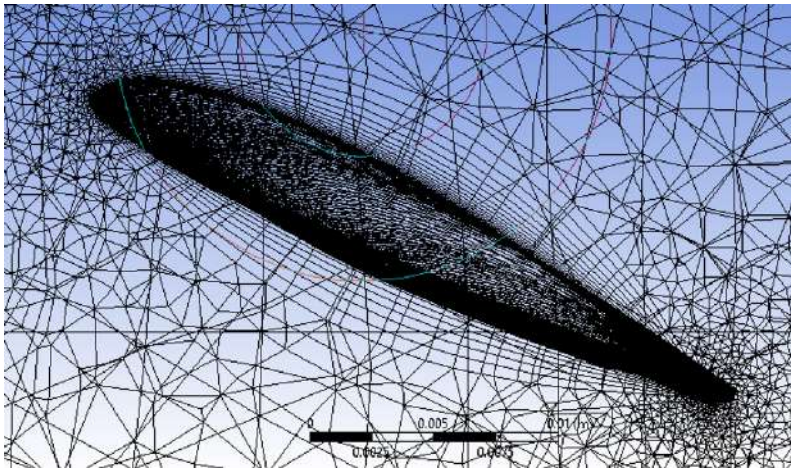

Figure 3.16: Boundary layer mesh at 75% of the blade radius.

The forthcoming Chapter will encompass an array of mesh investigations with the objective of attain-

ing meticulous and consistent results.

Chapter 4

Simulated Propeller Performance Results

In this Chapter, different studies and analyses will be conducted on the fluid domain previously discussed. These studies aim to find the model that represents the best flow conditions that will be imposed in the simulations. Numerical studies on the mesh refinement, turbulence model and rotating region will be carried out.

Finally, the performance results of the APC 14”x13” Sport and APC 10”x8” Sport commercial propellers will be presented and discussed. The results will be obtained through a low-fidelity numerical analysis based on the Blade Element theory introduced in Section 2.2 and through a high-fidelity numerical analysis carried out in ANSYS® Fluent®. The thrust and torque results will be plotted to interpret the aerodynamic performance of both propellers at different flight configurations.

4.1 Numerical Studies and Analyzed Propellers

To conduct a successful CFD analysis, it is essential to have a thorough understanding of the system’s physics and a detailed description of its geometry. In order to build the model that represents the best flow conditions and to obtain the most accurate possible results regarding each propeller’s performance, some studies should be made:

- **Mesh Refinement**: when conducting a numerical analysis, it is fundamental to maintain consistency in the simulation results regardless of the number of mesh cells used. Mesh refinement is a widely adopted method to achieve this, which involves progressively refining the model with increasingly finer meshes and comparing the performance results. This approach allows to determine the convergence of the solution with respect to mesh refinement. By examining various solutions, an asymptotic behavior can be observed and the changes in the outcomes for finer and finer meshes become less significant;
- **Turbulence Model**: it is important to note that there is no universal turbulence model that can

accurately predict performance in all flow conditions. In fact, for each specific flow condition, a more suitable turbulence model is required to provide accurate results. As detailed in Section 2.3, various turbulence models have been introduced for propeller flow analysis and will be now compared and investigated;

- **Rotating Region Sensitivity Analysis**: defining the dimensions of the rotating region is of paramount importance in order to avoid reversed flow scenarios, which have the potential to cause convergence issues and lead to unrealistic outcomes. Achieving accurate results requires ensuring that there are no significant radial gradients and that the dimensions of the rotating region are sufficient to facilitate proper evolution of the rotating flow in both the tangential and radial directions. As such, a thorough analysis of the dimensions of the rotating region is imperative.

As previously stated, this study aims to predict the performance of two commercial propellers. The subsequent illustrations showcase the quantitative analyses carried out for each commercial propeller model.

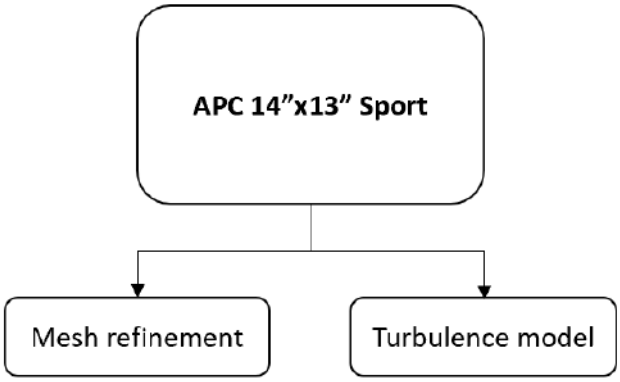

Figure 4.1: Numerical studies conducted on the model built for the APC 14”x13” Sport geometry.

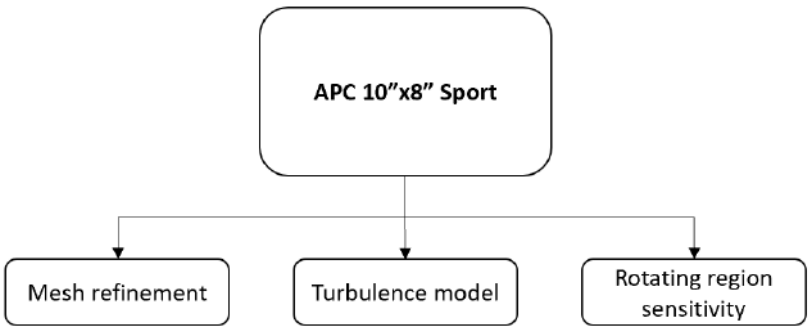

Figure 4.2: Numerical studies conducted on the model built for the APC 10”x8” Sport geometry.

4.2 Low-Fidelity vs High-Fidelity Numerical Analyses

In earlier sections, it was discussed that propeller performance can be predicted using various methods and approaches. These can be classified into low-fidelity numerical analyses and high-fidelity numerical analyses.

This work carried out a low-fidelity numerical analysis based on the Blade Element Theory. The performance results were obtained through JavaProp software. JavaProp [36] is a tool based on Blade Element Theory for the design and analysis of propellers and wind turbines. The implemented classical blade element design and analysis methods are based on coupling momentum considerations with 2D airfoil characteristics. It is, therefore, possible to consider different airfoil sections and the impact of their characteristics on the rotor performance. Nonetheless, the software does have its limitations:

- The disk-loading of the propeller must be lower than 2 ($C_T < 2$);
- The number of blades must be lower than 15 to avoid strong interactions due to thickness and overlapping;
- Three-dimensional and compressible flow effects are not taken into account.

This software allows the user to import a specific geometry of a blade and by defining the free stream velocity V_∞, the rotational propeller velocity Ω, the number of propeller blades B and its diameter D, it is possible to obtain the distribution of aerodynamic coefficients along the blade, as shown in Figure 4.3.

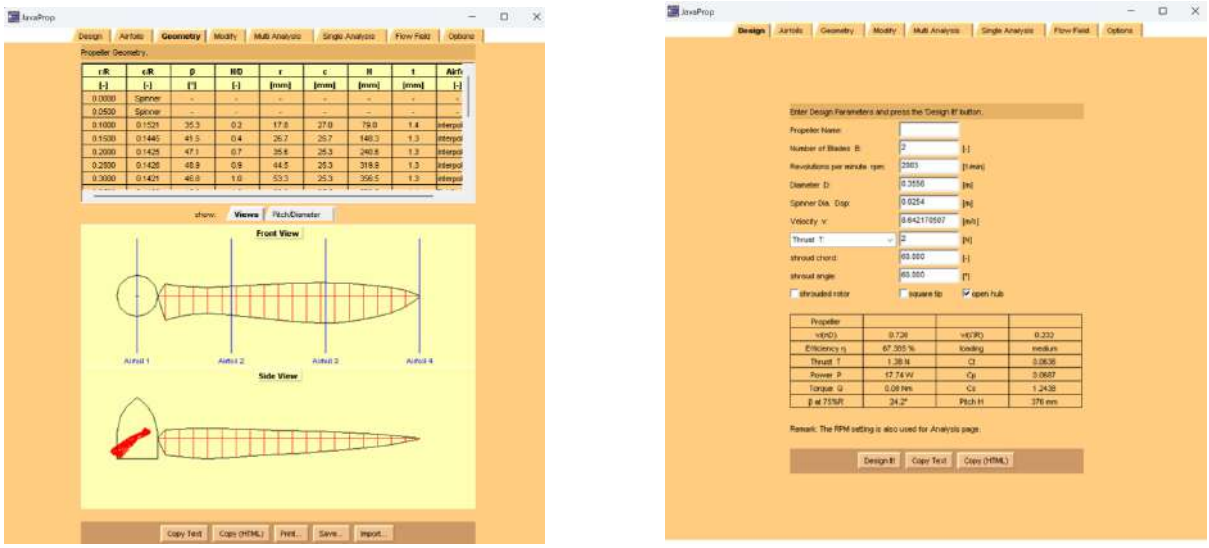

(a) Geometry.

(b) Inputs.

(c) Results.

Figure 4.3: JavaProp Interface. [36]

Furthermore, a high-fidelity numerical analysis was also performed recurring to ANSYS® Fluent® software and the methodology to obtain results regarding the propeller performance was explained in Chapter 3.

The results obtained through both low and high-fidelity numerical analyses will be presented in the following sections for both propellers: APC 14”x13” Sport and APC 10”x8” Sport.

4.3 Propeller 1: APC 14”x13” Sport

This Section will focus on the APC 14”x13” Sport propeller, which was the initial object of study. As previously mentioned, it boasts a 14-inch diameter and 13-inch pitch. In the previous Chapter, we explored the flow domain modeling process. In this Section, we will delve into the mesh refinement analysis and the turbulence model.

4.3.1 Mesh Refinement Analysis

The present study endeavors to determine the appropriate meshing by taking into account both convergence time and result accuracy. The aim is to achieve a balance between these two factors. It should be noted that augmenting the number of cells in the model may result in a lengthier solution convergence time, but it also leads to more precise results.

The mesh independence study for the APC 14”x13” propeller was carried out for the following conditions:

- Propeller angular velocity: $\Omega = 3003$ RPM;
- Advance ratio: $J = 0.581$ (Free stream velocity $V = 10.34\ m/s$).

The solutions of the thrust and torque were obtained for eight different cell element sizes as summarized in Table 4.1 and illustrated in Figure 4.4.

Table 4.1: Mesh refinement results. APC 14”x13” Sport.

cell element size (m)	number of cells	T (N)	Q (Nm)
0,0600	766 137	1,840	0,0751
0,0450	1 374 893	1,900	0,0913
0,0300	1 988 614	1,965	0,0934
0,0200	2 396 095	2,012	0,0954
0,0150	2 759 289	2,040	0,09635
0,0125	2 948 585	2,043	0,0966
0,0100	3 210 634	2,056	0,0966
0,0075	3 793 884	2,060	0,0967

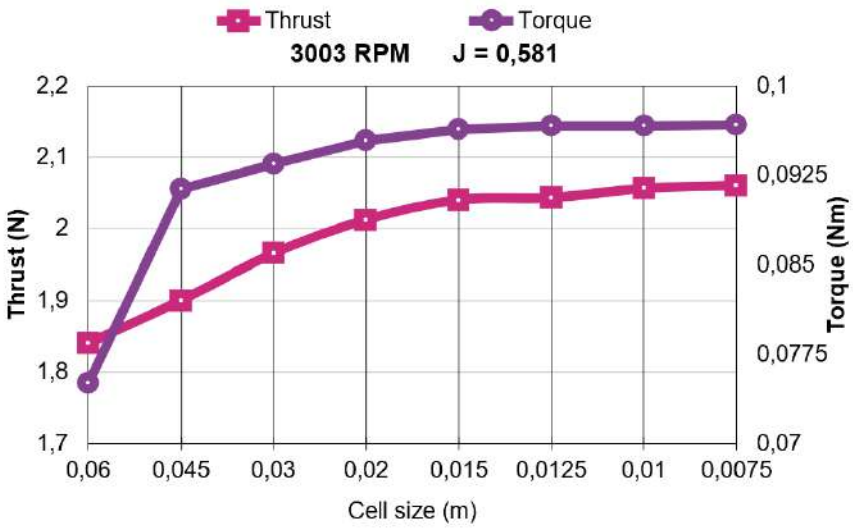

Figure 4.4: Mesh refinement results. APC 14”x13” Sport.

Based on the data presented, it is clear that implementing mesh refinement enhances the solution. Interestingly, the number of mesh cells does not seem to have any significant impact on the outcome as long as the element size is lower than 0.015 meters. Consequently, to ensure optimal outcomes while minimizing solution time, a thorough performance analysis was carried out using a model featuring a mesh element size equal to 0.01 meters.

Along with comparing the thrust and torque results, the values of the non-dimensional height of the first layer of the boundary layer around the propeller were also analyzed. Figure 4.5 illustrates the distribution of the parameter $y+$ along the blade, taking into account the selected mesh and flow conditions.

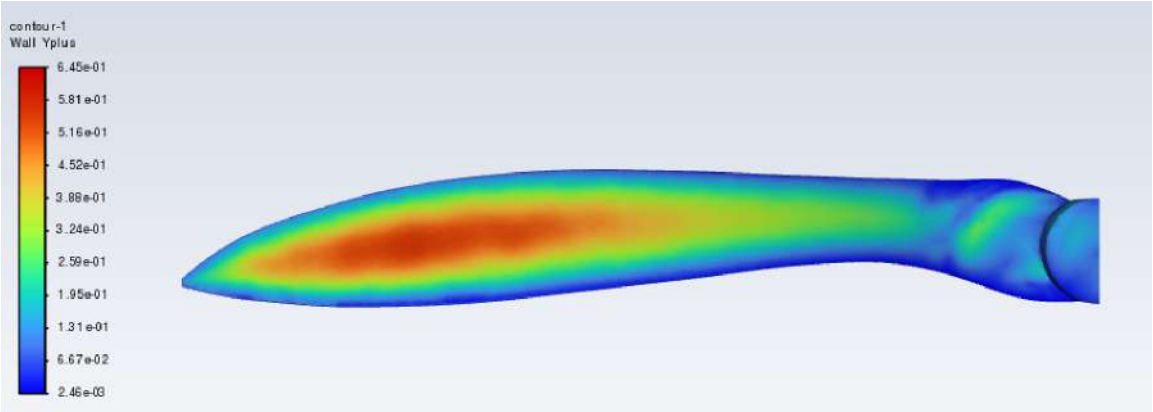

Figure 4.5: y+ contour of the propeller wall. APC 14"x13" Sport.

The highest value of $y+$ on the blade is 0.645, satisfying the requirement of being below 1.

4.3.2 Turbulence Model Analysis

For the mesh refinement study, the SST $k-\omega$ model was used, as it is the recommended model by ANSYS® Fluent®. Now, a different turbulence model, Standard $k-\epsilon$ is introduced and tested to evaluate its influence on the propeller performance.

The turbulence model study for the APC 14"x13" propeller was carried out for a rotational velocity of 2998 RPM. Table 4.2 presents the results obtained for both turbulence models.

Table 4.2: Turbulence model study. APC 14"x13" Sport.

2998 RPM	Experimental UIUC		Standard k-ε model		SST k-ω model	
J	c_T	c_Q	(%) ε_{ct}	(%) ε_{cq}	(%) ε_{ct}	(%) ε_{cq}
0,206	0,1133	0,0121	1,07	3,91	-5,79	3,85
0,277	0,1018	0,0122	-1,59	5,84	-8,28	0,36
0,31	0,1137	0,0120	-2,74	6,32	-9,04	-1,37
0,381	0,1133	0,0120	-3,79	4,59	-8,37	-5,87
0,412	0,1098	0,0121	-3,83	3,47	-7,94	-6,36
0,485	0,1075	0,0122	-4,19	2,26	-8,40	-8,14
0,553	0,0928	0,0120	-0,68	1,41	-8,16	-8,72
0,617	0,0833	0,0116	1,25	1,76	-6,72	-8,36

After analyzing the results, it can be seen that both models have a tendency to underpredict the thrust when compared to experimental results. However, the Standard $k-\epsilon$ model tends to overpredict the torque, whereas the SST $k-\omega$ model tends to underpredict it.

Note that the formulas for the torque and thrust errors are:

$$(\%)\epsilon_{ct} = \frac{c_{Tcfd} - c_{Texperimental}}{c_{Texperimental}} \times 100 \qquad (\%)\epsilon_{cq} = \frac{c_{Qcfd} - c_{Qexperimental}}{c_{Qexperimental}} \times 100 \qquad (4.1)$$

In conclusion, both models accurately depict the flow conditions around the rotating propeller. However, the Standard $k-\epsilon$ model produces more accurate results. Therefore, the remaining performance

analyses will be conducted using the Standard $k - \epsilon$ turbulence model.

4.3.3 Performance at 2003 RPM

Vertical climb flight simulations were carried out using a mesh with around 3 200 000 cells and using the Standard $k - \epsilon$ turbulence model.

Figure 4.6 shows the comparisons of the results obtained through JavaProp, ANSYS® Fluent® and the experimental testing [7] for a rotational propeller velocity equal to 2003 RPM.

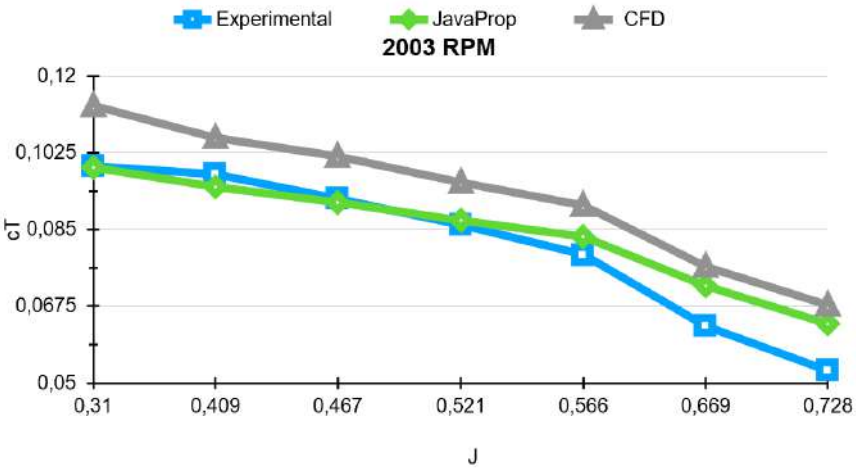

(a) Thrust coefficient.

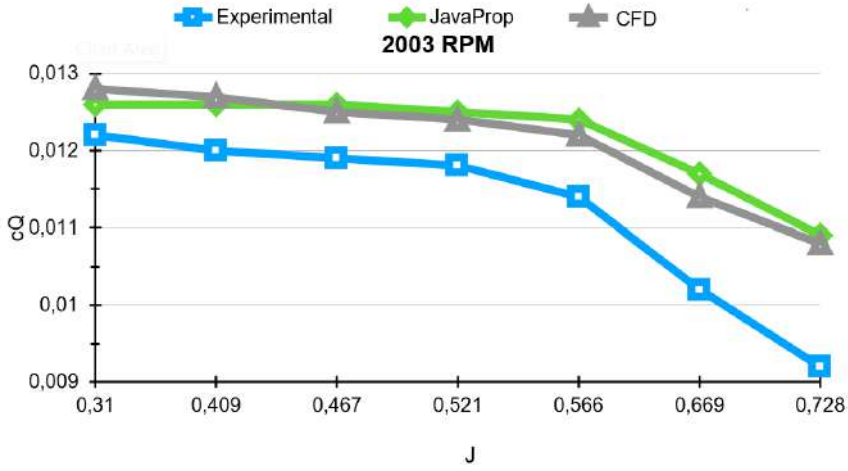

(b) Torque coefficient.

Figure 4.6: Performance. $\Omega = 2003$ RPM. APC 14"x13" Sport.

Table 4.3 presents the error of the results obtained with both low and high-fidelity numerical methods and the comparison with the experimental testing conducted at UIUC.

Table 4.3: Error comparison between high-fidelity and low-fidelity analyses. $\Omega = 2003$ RPM. APC 14"x13" Sport.

2003 RPM	Experimental UIUC		CFD		JavaProp	
J	c_T	c_Q	(%) ε_{ct}	(%) ε_{cq}	(%) ε_{ct}	(%) ε_{cq}
0,31	0,0994	0,0122	13,91	4,82	-0,28	3,39
0,409	0,0976	0,0120	8,52	5,42	-2,98	5,04
0,467	0,0920	0,0119	10,54	5,12	-0,91	5,37
0,521	0,0861	0,0118	11,20	4,58	1,17	5,94
0,566	0,0792	0,0114	14,12	6,34	5,13	8,34
0,669	0,0630	0,0102	21,58	11,78	14,51	13,86
0,728	0,0528	0,0092	28,41	17,15	20,42	18,64

Upon examining the errors presented, it is apparent that ANSYS® Fluent® overestimated both thrust and torque. The maximum inconsistency is 28,41% for the thrust coefficient and 17,15% for the torque coefficient, both of which occur at an advance ratio of 0,728. On average, there is a 15,5% error for the thrust coefficient and a 7,89% error for the torque coefficient. Additionally, as discussed in Section 2.2, the thrust increases with the lift and decreases with the drag coefficient, while the torque decreases with both lift and drag. Given that both coefficients are overestimated, it is possible that the lift is being overpredicted and/or the drag is being underestimated.

In contrast, the data gathered through JavaProp, which uses the Blade Element Theory, aligns more closely with the results from experimentation ([7]). The differences are minimal, with a maximum deviation of 20,42% for the thrust coefficient and 18,64% for the torque coefficient. On average, there is only a 5,29% error in the thrust coefficient and an 8,65% error in the torque coefficient.

In both analyses, there is a clear correlation between the error and the advance ratio. As the value of J increases, the accuracy of the results for both thrust and torque coefficients decreases.

4.3.4 Performance at 2508 RPM

Figure 4.7 shows the comparisons of the results obtained through JavaProp and ANSYS® Fluent® and the experimental testing for a rotational propeller velocity of 2508 RPM.

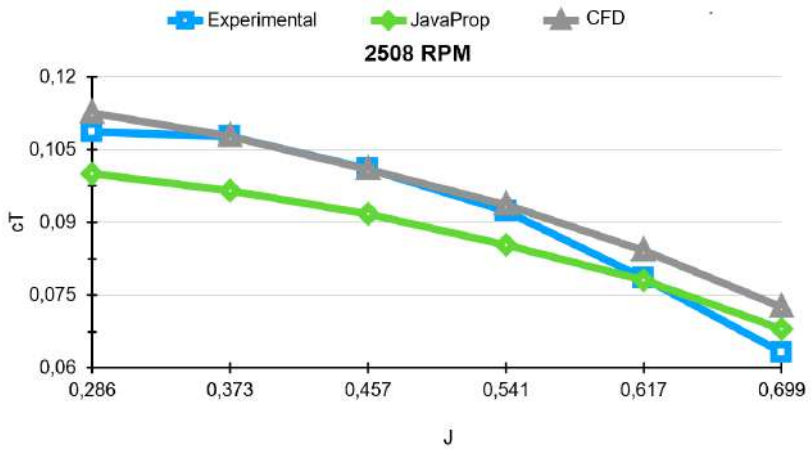

(a) Thrust coefficient.

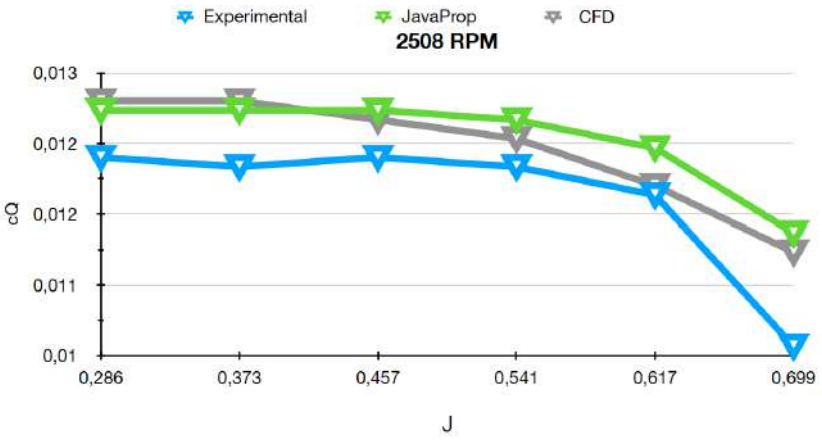

(b) Torque coefficient.

Figure 4.7: Performance. $\Omega = 2508$ RPM. APC 14”x13” Sport.

Table 4.4 provides the relative errors of both high-fidelity and low-fidelity numerical analyses, respectively.

Table 4.4: Error comparison between high-fidelity and low-fidelity analyses. $\Omega = 2508$ RPM. APC 14”x13” Sport.

2508 RPM	Experimental UIUC		CFD		JavaProp	
J	c_T	c_Q	(%) ε_{ct}	(%) ε_{cq}	(%) ε_{ct}	(%) ε_{cq}
0,286	0,1087	0,0121	3,54	4,88	-7,98	3,88
0,373	0,1078	0,0120	-0,09	5,17	-10,48	4,47
0,457	0,1011	0,0121	-0,18	2,98	-9,17	3,69
0,541	0,0923	0,0120	1,49	2,03	-7,45	3,86
0,617	0,0785	0,0117	7,20	0,88	-0,52	3,52
0,699	0,0632	0,0101	14,66	9,91	7,67	11,71

The table above displays the accuracy of two analyses, with ANSYS® Fluent® providing superior solutions for predicting propeller performance. In the high-fidelity analysis, the maximum error is 14,66% for the thrust coefficient and 9,91% for the torque coefficient at an advance ratio of 0,699. Compared to the results at a rotational speed of 2003 RPM, the solution now provides a more accurate representation of the actual flow.

The low-fidelity analysis continues to provide accurate results; the highest deviation is -10,48% for the thrust coefficient and 11,71% for the torque coefficient. The average error recorded is 4,66% for the thrust coefficient and 4,55% for the torque coefficient.

Furthermore, both analyses display a sudden increase in error when the free stream velocity and advance ratio reach their peak points. Similar to the findings at a rotational velocity of 2003 RPM, an increase in the advance ratio (and free stream velocity) leads to a decline in both the thrust and torque coefficients.

4.3.5 Performance at 2998 RPM

Figure 4.8 shows the comparisons of the results obtained through JavaProp and ANSYS® Fluent® and the experimental testing for a rotational propeller velocity equal to 2998 RPM.

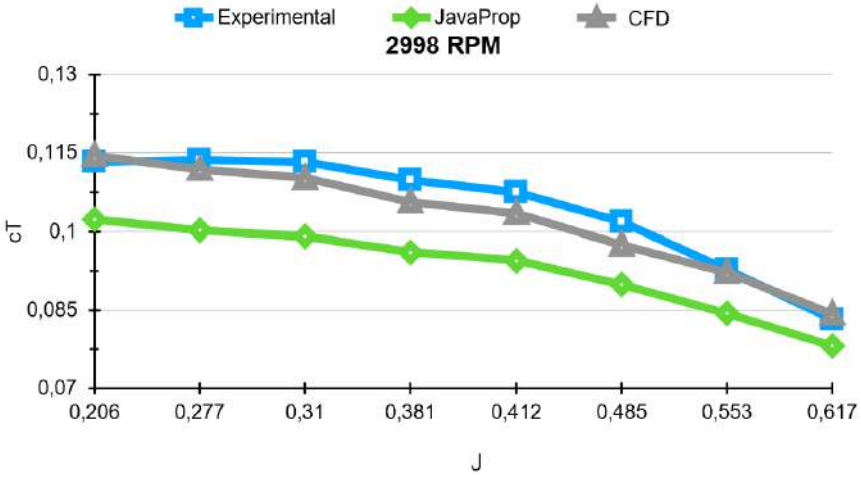

(a) Thrust coefficient.

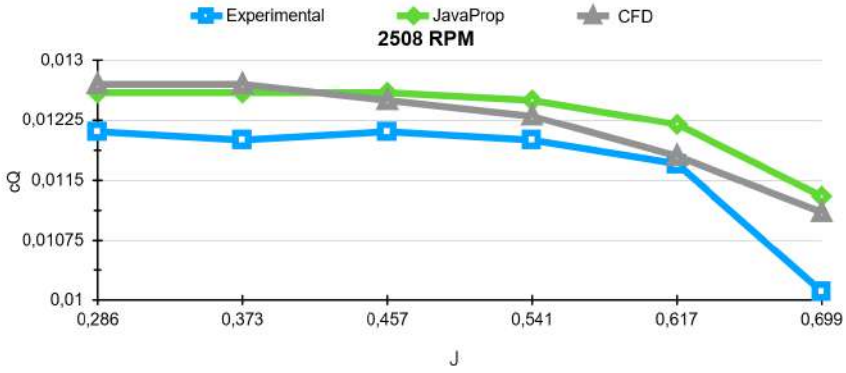

(b) Torque coefficient.

Figure 4.8: Performance. $\Omega = 2998$ RPM. APC 14"x13" Sport.

Table 4.5 provides the relative errors of both high-fidelity and low-fidelity numerical analyses, respectively.

Table 4.5: Error comparison between high-fidelity and low-fidelity analyses. $\Omega = 2998$ RPM. APC 14"x13" Sport.

2998 RPM	Experimental UIUC		CFD		JavaProp	
J	c_T	c_Q	(%) ε_{ct}	(%) ε_{cq}	(%) ε_{ct}	(%) ε_{cq}
0,206	0,1133	0,0121	1,07	3,91	-9,67	5,40
0,277	0,1137	0,0120	-1,59	5,84	-11,82	5,82
0,310	0,1133	0,0120	-2,74	6,32	-12,52	5,46
0,381	0,1098	0,0121	-3,79	4,59	-12,47	4,00
0,412	0,1075	0,0122	-3,83	3,47	-12,07	3,68
0,485	0,1018	0,0122	-4,19	2,26	-11,71	3,15
0,553	0,0928	0,0120	-0,68	1,41	-9,11	3,68
0,617	0,0833	0,0116	1,25	1,76	-6,25	4,51

It can be seen that ANSYS® Fluent® accurately predicted the flow properties of the rotating propeller for the referred conditions, with the thrust and torque coefficients showing results similar to those obtained through experimental testing. The maximum level of inconsistency was -4,19% for the thrust coefficient and 6,3% for the torque coefficient.

In contrast, the low-fidelity analysis significantly underestimated the thrust and overestimated the torque, with an average error of -10,70% for the thrust coefficient and 4,46% for the torque coefficient.

4.3.6 Performance at 3508 RPM

Figure 4.9 show the comparisons of the results obtained through JavaProp and ANSYS® Fluent® and the experimental testing for a rotational propeller velocity of 3508 RPM.

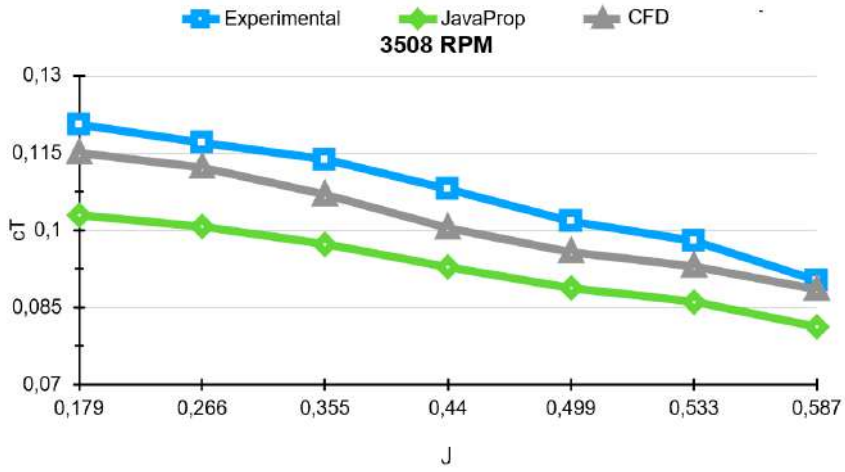

(a) Thrust coefficient.

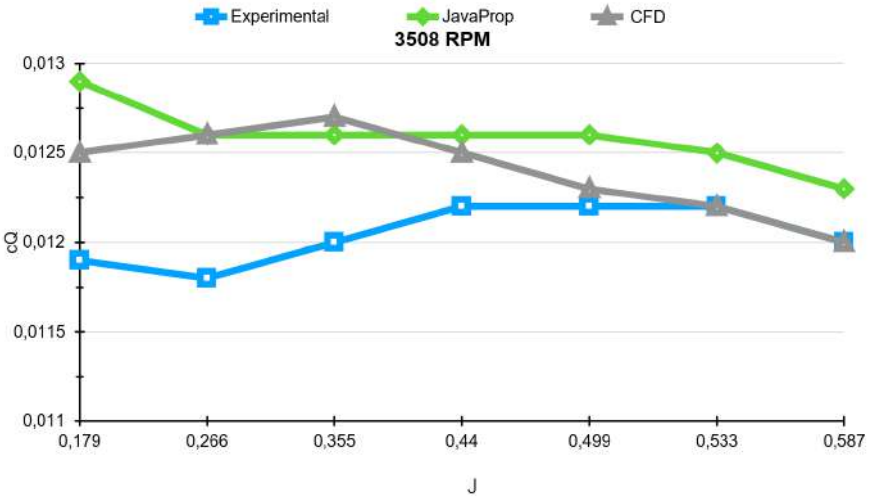

(b) Torque coefficient.

Figure 4.9: Performance. $\Omega = 3508$ RPM. APC 14"x13" Sport.

Table 4.6 provides the relative errors of both high-fidelity and low-fidelity numerical analyses, respectively.

Table 4.6: Error comparison between high-fidelity and low-fidelity analyses. $\Omega = 3508$ RPM. APC 14"x13" Sport.

3508 RPM	Experimental UIUC		CFD		JavaProp	
J	c_T	c_Q	(%) ε_{ct}	(%) ε_{cq}	(%) ε_{ct}	(%) ε_{cq}
0,179	0,1205	0,0119	-4,59	4,64	-14,61	7,84
0,266	0,1170	0,0118	-4,09	7,13	-13,97	7,47
0,355	0,1137	0,0120	-6,00	5,55	-14,44	5,11
0,440	0,1080	0,0122	-7,04	2,32	-13,97	3,02
0,499	0,1017	0,0122	-5,81	1,15	-12,65	2,97
0,533	0,0979	0,0122	-5,05	0,51	-12,03	2,85
0,587	0,0903	0,0120	-1,96	0,36	-9,96	2,73

Based on the previous data, the high-fidelity analysis solution is underestimating the thrust and overestimating the torque. In fact, the maximum error for the thrust coefficient is -7,04%, while the torque coefficient has a maximum error of 7,13%. However, it's worth noting that the accuracy of the torque results improves as the advance ratio increases.

Alternatively, the results from JavaProp software demonstrate a significant underestimation of thrust and overestimation of torque. The thrust coefficient has a maximum inconsistency of -14,44%, while the torque coefficient has a maximum inconsistency of 7,84%. Nevertheless, as with the high-fidelity analysis solution, the accuracy of both thrust and torque solutions improves with higher advance ratios.

Upon comparing the data presented in Tables 4.3, 4.4, 4.5, and 4.6, it becomes apparent that the accuracy of CFD simulations is consistently high, with the exception of instances when the rotational velocity is at its lowest. In such cases, the accuracy of the simulations experiences a notable decrease.

In contrast, as the rotational velocity of the propeller increases, Blade Element Theory is proven to be less accurate. This is due to flow disruptions that cannot be predicted by the theory, caused by an increase in the flow velocity around the propeller ([37]).

Based on the results, it has been observed that in the case of lower Reynolds numbers, low-fidelity numerical analysis can be more accurate than high-fidelity analysis. However, as the Reynolds number increases and vorticity and turbulence become more prominent, ANSYS® Fluent® proves to be an effective tool for predicting propeller performance.

By altering the flow conditions, one can examine the diverse flow properties. As depicted in Figure 4.10, the total pressure contours on the propellers' blades are observed when the rotational velocity is 2508 RPM and J=0,286 and 3508 RPM and J=0,587.

In both of the aforementioned configurations, it is noted that the high-pressure regions of the blades reside towards the tips and trailing edges, while the low-pressure regions are situated towards the leading edges. The increase in rotating velocity and free stream velocity leads to an increase in the absolute total pressure felt at the tip of the blades.

Figure 4.11 shows the axial velocity field for both flight configurations: when $\Omega = 2508$ RPM and J=0,286 and when $\Omega = 3508$ RPM and J=0,587, respectively.

As the free stream velocity increases, the axial velocity field experiences elevated values. It should be noted that at the tip of the blades, the axial velocity moves in the opposite direction of the free stream.

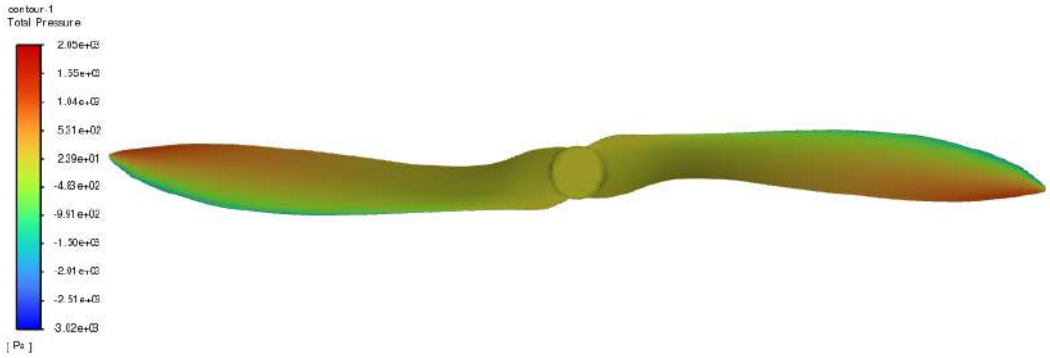

(a) $\Omega = 2508$ RPM and J=0,286.

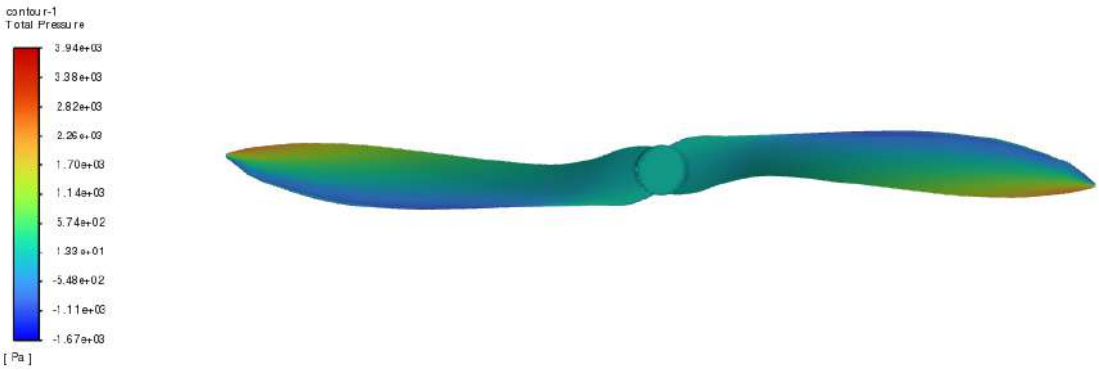

(b) $\Omega = 3508$ RPM and J=0.587.

Figure 4.10: Total pressure contour on the propeller wall. APC 14"x13" Sport.

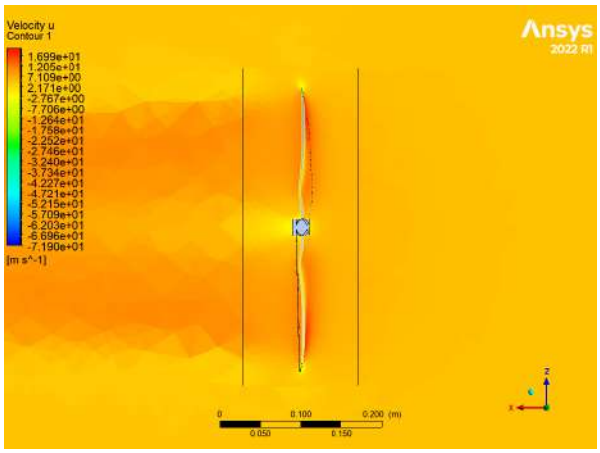

(a) $\Omega = 2508$ RPM and J=0,286.

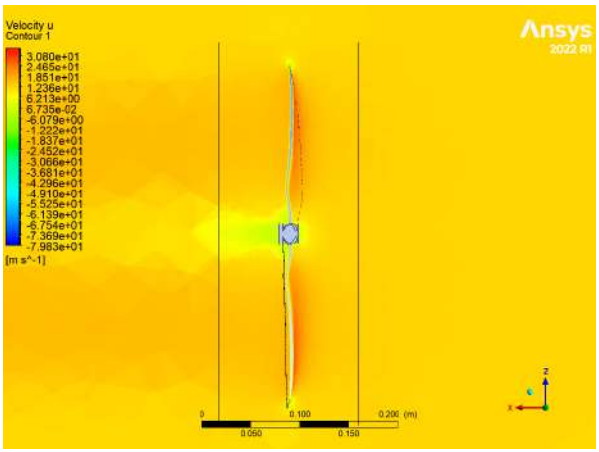

(b) $\Omega = 3508$ RPM and J=0,587.

Figure 4.11: Axial velocity distribution. APC 14"x13" Sport.

Refer to Figure 4.12 for a clear visualization of these streamlines at $\Omega = 3508$ RPM and J=0,587, where it is possible to observe the streamlines' rotating behavior around the rotating propeller and at the outlet section.

Furthermore, Figure 4.13 presents the distribution of viscosity around the rotating propeller. Based on observation, it is apparent that the second flight configuration does not yield the same outcome of a turbulent wake following the propeller's rear walls compared to the first configuration. This can be attributed to the heightened free stream and rotational velocities, leading to a reduction in viscosity.

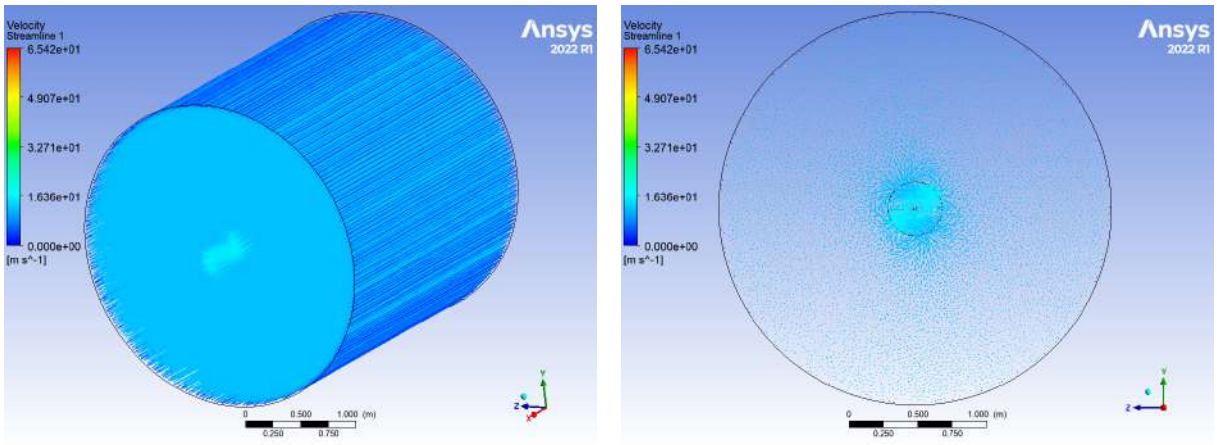

Figure 4.12: Streamlines on both domains when $\Omega = 3508$ RPM and J=0,587. APC 14”x13” Sport.

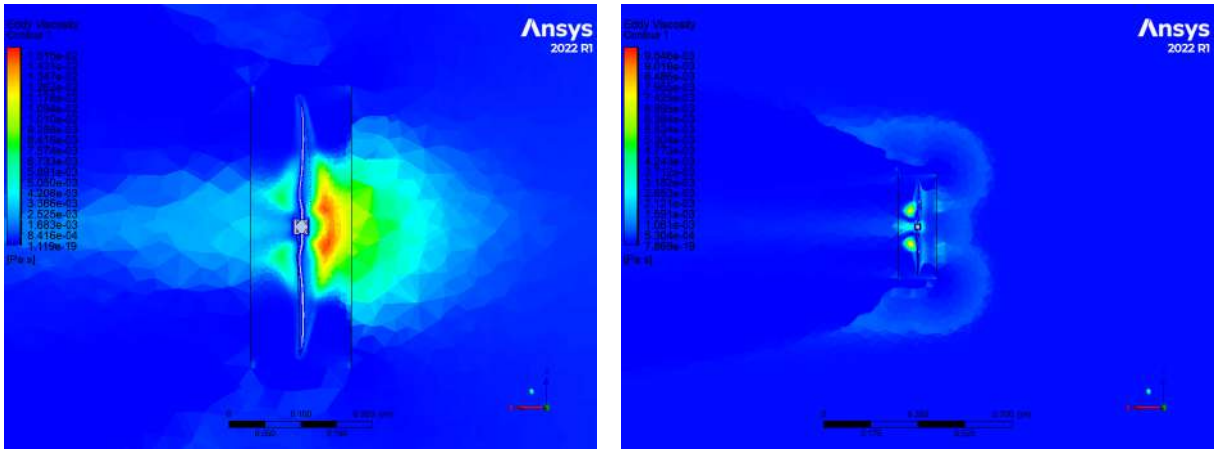

(a) $\Omega = 2508$ RPM and J=0,286.

(b) $\Omega = 3508$ RPM and J=0,587.

Figure 4.13: Eddy viscosity distribution. APC 14”x13” Sport.

4.4 Propeller 2: APC 10”x8” Sport

Similar studies to the ones conducted with the APC 14”x13” Sport model were also conducted for the APC 10”x8” Sport propeller.

4.4.1 Mesh Refinement Analysis

The mesh refinement study will be different from the one conducted with the 14”x13” propeller. Instead of analyzing the convergence of the torque and thrust, an analysis of the accuracy of these parameters is carried out. Hence, three different meshes, summarized in Table 4.7 and shown in Figure 4.14, are generated and investigated.

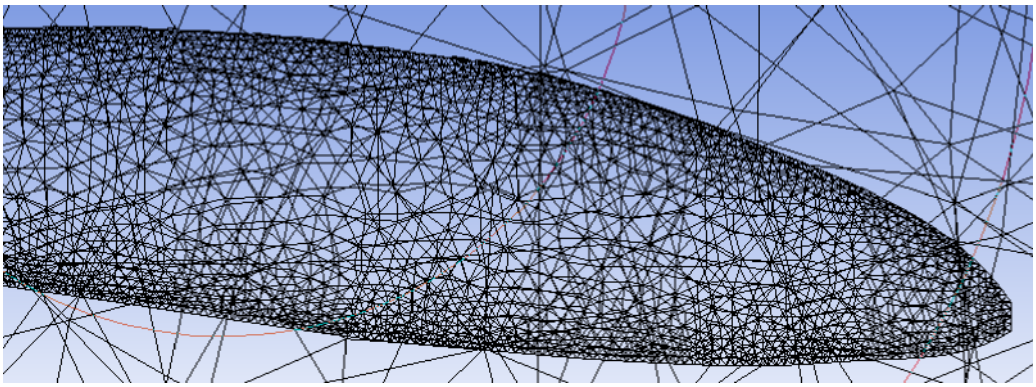

(a) Coarse mesh.

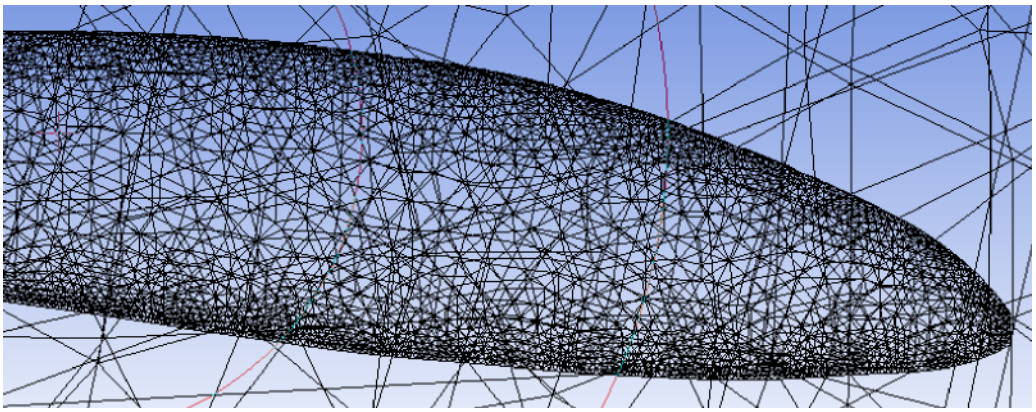

(b) Medium mesh.

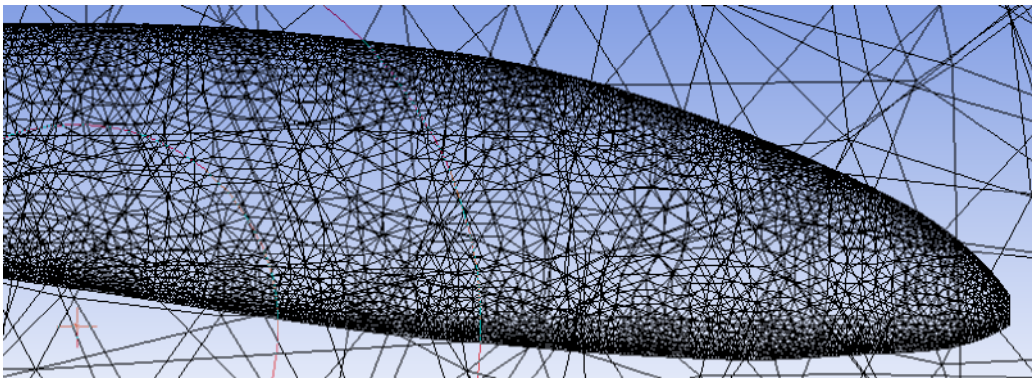

(c) Fine mesh.

Figure 4.14: Mesh refinement. APC 10”x8” Sport.

Table 4.7: Mesh refinement study. APC 10”x8” Sport.

Mesh	Cell element size (m)	Number of cells
Coarse	0,055	629 411
Standard	0,04	1 085 187
Fine	0,0275	1 994 231

In all three meshes, there was a focus on improving the leading and trailing edges. This is crucial for

accurately capturing areas with high curvature.

This mesh refinement study was conducted for the following flow conditions:

- Propeller Angular Velocity: $\Omega = 3900$ RPM;
- Advance Ratio: $J = 0$ (Free Stream Velocity $V = 0$).

The thrust and torque coefficients obtained are summarized in Table 4.8. The errors relative to the experimental testing conducted at UIUC are also presented. For the aforementioned conditions, the experimental thrust and torque coefficients are 0,1089 and 0,01114, respectively.

Table 4.8: Mesh refinement results. APC 10"x8" Sport.

Mesh	C_T	$(\%)\epsilon_{ct}$	C_Q	$(\%)\epsilon_{cq}$
Coarse	0,1054	-3,24	0,01235	10,89
Standard	0,1080	-0,85	0,01170	4,98
Fine	0,1091	0,17	0,01097	-1,57

It is evident that the finer grid yields the most precise outcomes in comparison to the experimental testing. Thus, to evaluate the performance of the APC 10"x8" Sport propeller, the simulations were carried out using a model with a mesh element size equal to 0,0275 meters.

In addition to the comparison of thrust and torque, the non-dimensional height of the first layer of the boundary layer around the propeller was also analyzed. For the selected mesh and the referred flow conditions, Figure 4.15 shows the distribution of the parameter $y+$ along the blade.

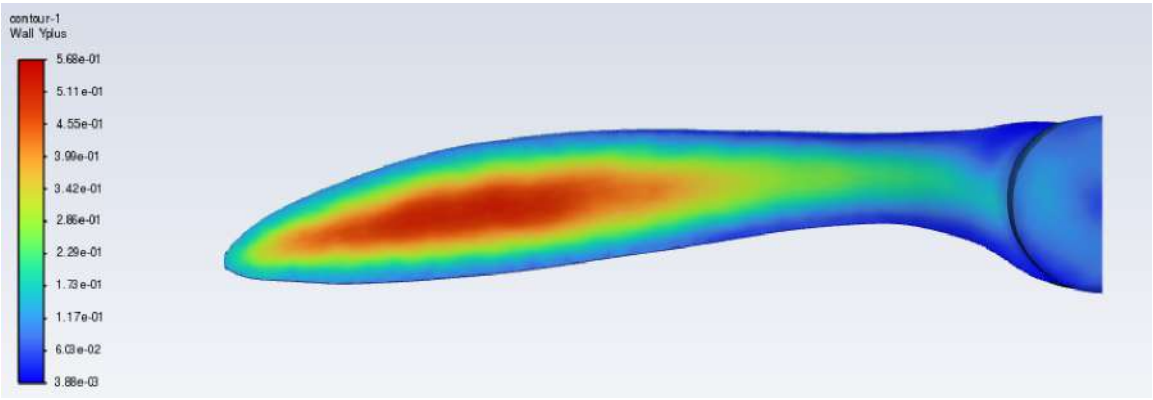

Figure 4.15: y+ contour of the propeller wall. APC 10"x8" Sport.

The value of $y+$ reaches its maximum at 0,568 along the blade, which satisfies the condition of being below 1.

4.4.2 Turbulence Model Analysis

A mesh refinement study was performed using the SST $k-\omega$ turbulence model, similar to the analysis conducted for the APC 14"x13" propeller. Now, three additional turbulence models are introduced.

The turbulence study for the APC 10"x8" propeller was carried out for a rotational propeller velocity equal to 3900 RPM. Table 4.9 presents the results obtained for the different turbulence models.

Table 4.9: Turbulence model study. APC 10"x8" Sport.

Turbulence model	C_T	$(\%)\epsilon_{ct}$	C_Q	$(\%)\epsilon_{cq}$
Standard $k-\epsilon$	0,1176	8,01	0,0111	-0,56
Realizable $k-\epsilon$	0,1240	13,90	0,0105	-5,81
SST $k-\omega$	0,1091	0,17	0,01097	-1,57
Standard $k-\omega$	0,1030	-5,46	0,0125	11,87

The predictions made by both $k-\epsilon$ models regarding the thrust are higher than the experimental testing, with the Realizable model having an error over 10%. On the other hand, the Standard $k-\omega$ model overestimates the torque. The SST $k-\omega$ model provides the most accurate results, making it the preferred option for the remaining simulations and a precise representation of the real flow conditions.

It should be noted that the APC 14"x13" Sport propeller's turbulence model with the best results was the Standard $k-\epsilon$. This highlights the fact that there is no universal turbulence model as each model has its own advantages and disadvantages, and the accuracy of the model depends on the flow conditions.

4.4.3 Rotating Region Sensitivity Analysis

The choice of dimensions for the rotating domain may vary depending on the author and the nature of the investigation. For instance, in a study conducted by Kutty and Rajendran, the dimensions for the height and diameter of the domain were set at 0,4D and 1,1D respectively, as cited in [14]. On the other hand, Mehdipour's investigation [38] employed dimensions of 0,38D and 1,15D, where D denotes the diameter of the propeller.

To obtain an accurate depiction of the flow conditions surrounding the rotating propeller, various combinations of height and length values for the regions were tested (for the same flow conditions as in the turbulence model study). The outcomes of changing the height of the rotating fluid domain are displayed in Table 4.10.

Table 4.10: Rotating region height sensitivity analysis. APC 10"x8" Sport.

Height	C_T	$(\%)\epsilon_{ct}$	C_Q	$(\%)\epsilon_{cq}$
0,2D	0,1057	-2,98	0,0106	-4,69
0,4D	0,1091	0,17	0,01097	-1,57
0,6D	0,1084	-0,43	0,0109	-1,91

When compared to the other options, there is a clear decrease in both thrust and torque when the height is the lowest. Both cases of 0,4D and 0,6D provide similar results, making little difference in

the increase of height. However, for real applications, it is convenient to maintain the rotating region enclosing the propeller of study as small as possible.

An analysis was conducted on the diameter of the rotating region, and the resulting data is presented in Table 4.11 for various changes in the diameter of the rotating fluid domain.

Table 4.11: Rotating region diameter sensitivity analysis. APC 10"x8" Sport.

Diameter	C_T	$(\%)\epsilon_{ct}$	C_Q	$(\%)\epsilon_{cq}$
1,05D	0,1066	-2,13	0,01093	-2,56
1,1D	0,1091	0,17	0,01097	-1,57
1,15D	0,1082	-0,68	0,01089	-2,23
1,2D	0,1083	-0,51	0,01089	-2,23

As the diameter of the rotating region increases, it is noticeable that the thrust and torque solutions converge. The most significant difference is observed between cases 1,05D and 1,1D, while the differences between the other cases are negligible. Therefore, all cases provide precise approximations of the actual conditions.

Concluding the analysis, both cases 0,4D for the height and 1,1D for the diameter provide closer results to the experimental ones. Hence, the simulations were carried out using a rotating region of diameter equal to 1,1D and height equal to 0,4D.

4.4.4 Performance at Hovering Conditions

In this Section, the performance of the APC 10"x8" Sport propeller will be studied. It has a smaller diameter and pitch when compared to the APC 14"x13" Sport propeller. According to Equation (2.17), the thrust is affected by both the diameter and pitch. The torque coefficient also follows the same pattern. Therefore, it is anticipated that there will be a decline in both thrust and torque.

Hovering flight simulations (J=0, i.e., free stream velocity equal to zero) were carried out using a mesh of around 2 million cells and using the SST $k-\omega$ turbulence model. Figure 4.16 shows the results for thrust and torque, respectively, obtained through JavaProp, ANSYS® Fluent® and the experimental testing ([7]) when J=0.

It is clear that an increase in the rotational velocity of the propeller results in a corresponding increase in both the torque and thrust generated. Table 4.12 provides the relative errors of both high-fidelity and low-fidelity analyses, respectively.

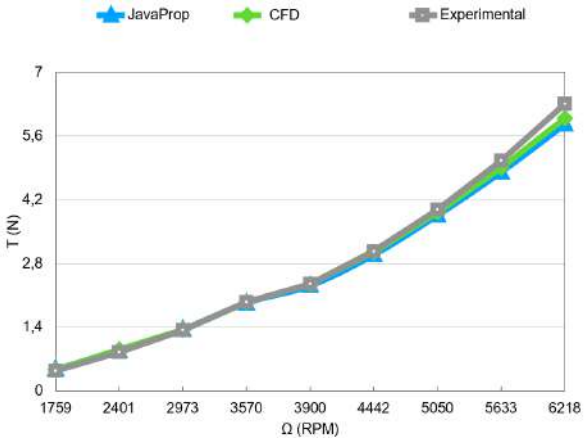

(a) Thrust.

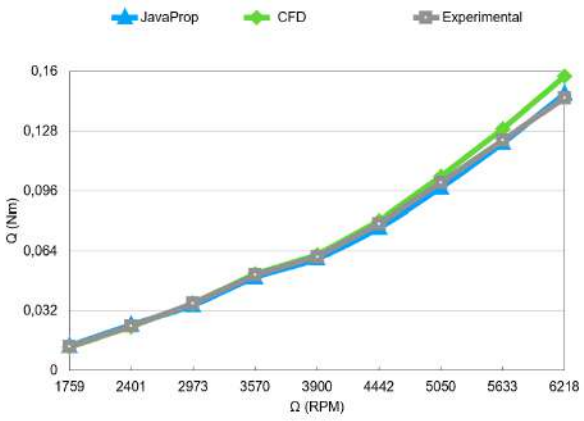

(b) Torque.

Figure 4.16: Performance. APC 10"x8" Sport.

Table 4.12: Error comparison between high-fidelity and low-fidelity analyses. APC 10"x8" Sport.

	Experimental UIUC		CFD		JavaProp	
Ω (RPM)	T (N)	Q (Nm)	(%) ε_T	(%) ε_Q	(%) ε_T	(%) ε_Q
1759	0,44	0,0128	4,38	2,08	5,94	-1,33
2401	0,85	0,0238	6,68	2,53	2,20	-1,47
2973	1,33	0,0359	1,19	-2,59	0,85	0,06
3570	1,95	0,0512	-0,25	-2,84	-1,20	1,34
3900	2,35	0,0610	0,17	-1,58	-1,74	1,49
4442	3,07	0,0785	-0,60	-2,70	-2,55	2,22
5050	3,98	0,1005	-1,66	-2,65	-2,99	3,26
5633	5,06	0,1232	-3,01	-1,28	-4,97	4,78
6218	6,31	0,1459	-4,89	1,45	-7,12	7,80

Based on the CFD simulations' results, the maximum error observed was -4,89% for the thrust coefficient and -2,84% for the torque coefficient. On average, the error was found to be 0,22% for the thrust coefficient and -0,84% for the torque coefficient. For low angular velocities, the thrust and torque are overpredicted. Once the angular velocity of the propeller is increased, it is possible to visualize a tendency to underpredict both thrust and torque. Overall, the analysis has demonstrated its ability to accurately predict flow properties across all configurations.

In contrast, when using low-fidelity numerical analysis, the maximum error for the thrust coefficient is -7,12% and for the torque coefficient it is 7,80%. Additionally, the average error for the thrust coefficient is -1,29% and for the torque coefficient it is 2,02%. While the accuracy of these results is not as high as those obtained with ANSYS® Fluent®, the Blade Element Theory is still an effective method for predicting the performance of a rotating propeller.

Figure 4.17 portrays the pressure contours on the front walls of the blades when the rotational velocity is equal to 1759 RPM and 6218 RPM, respectively. The impact of rotational speed on pressure levels is clearly discernible, as evidenced by the expansion of the pressure range from $[-298, 513]$ Pascal to $[-6200, 6430]$ Pascal.

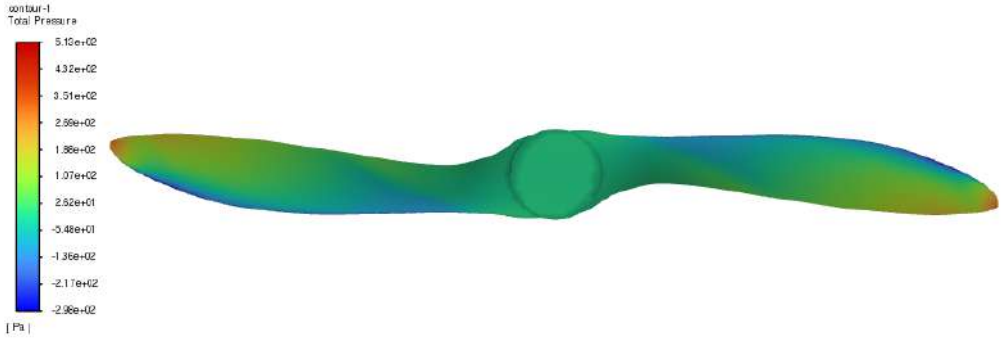

(a) $\Omega = 1759$ RPM.

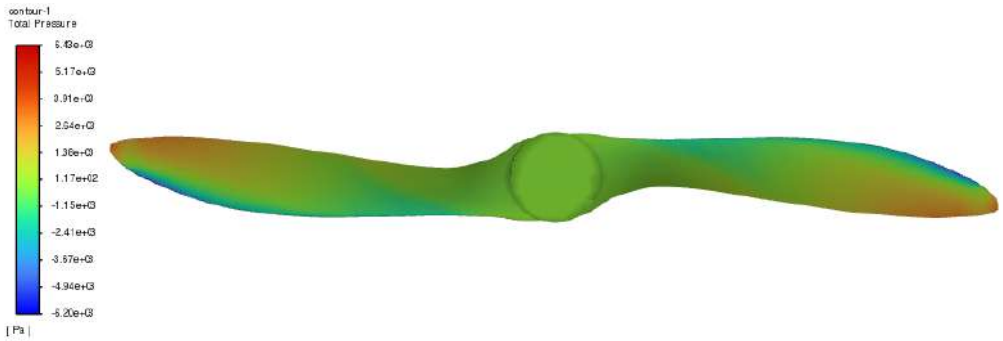

(b) $\Omega = 6218$ RPM.

Figure 4.17: Total pressure contour on the propeller wall. APC 10”x8” Sport.

The axial velocity around the rotating propeller in both the rotating and static fluid domains is depicted in Figure 4.18. The two graphs illustrate the velocity when the angular velocity is 1759 RPM and 6218 RPM, respectively. As the angular velocity increases, the range of values for the axial velocity also expands. Notably, velocity peaks can be observed along the front wall of the blades. In each blade, there is a positive peak at approximately 30% of the radius and a negative peak near the tips.

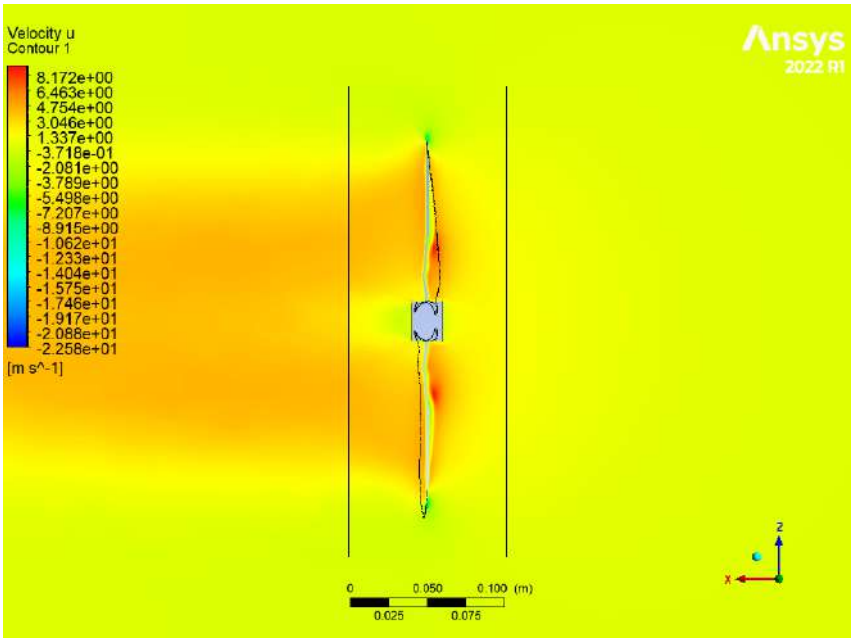

(a) $\Omega = 1759$ RPM.

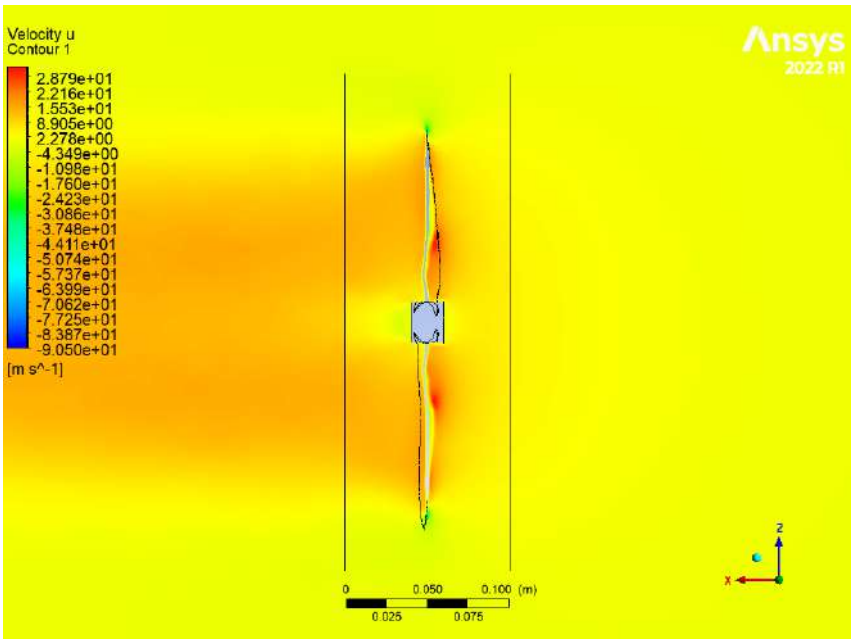

(b) $\Omega = 6218$ RPM.

Figure 4.18: Axial velocity distribution. APC 10"x8" Sport.

Figure 4.19 displays additional details that can be observed in the streamlines across both domains at $\Omega = 1759$ RPM.

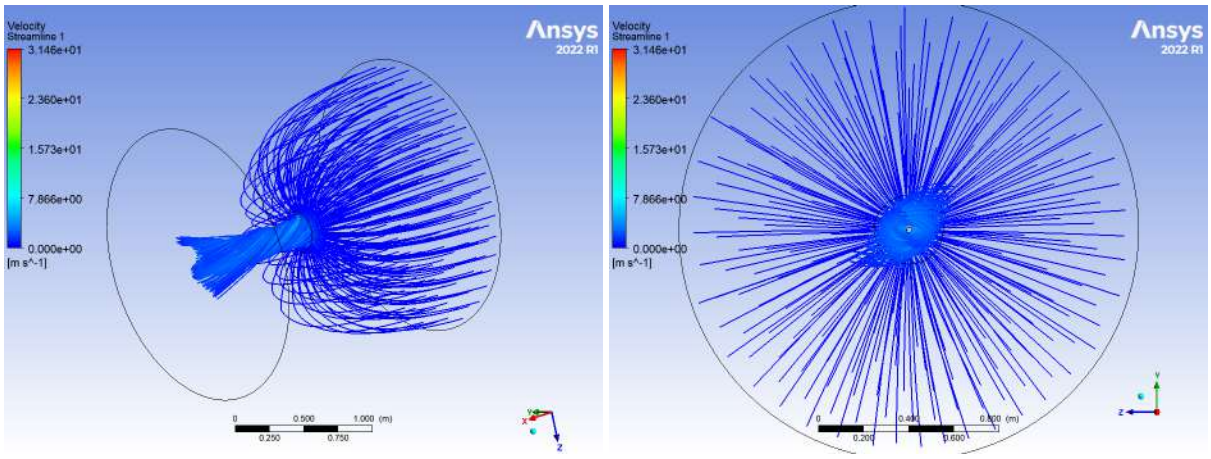

Figure 4.19: Streamlines on both domains when $\Omega = 1759$ RPM. APC 10"x8" Sport.

The comparison of Figures 4.12 and 4.19 presents an intriguing observation regarding the distinct behaviors of the streamlines based on the specific flight configuration. The former scenario portrays vertical climb flight, while the latter scenario illustrates hovering (J=0).

Lastly, the eddy viscosity field around the rotating propeller is shown in Figure 4.20. Both illustrations depict the progression of flow and the fully-formed turbulent wake behind the propeller's rear walls. As the rotational velocity increases, the range of values expands accordingly. Notably, there exists a discernible difference between the flow depicted in this scenario and the turbulent flow illustrated in Figure 4.13. The formation of the turbulent wake is more pronounced in hovering configurations.

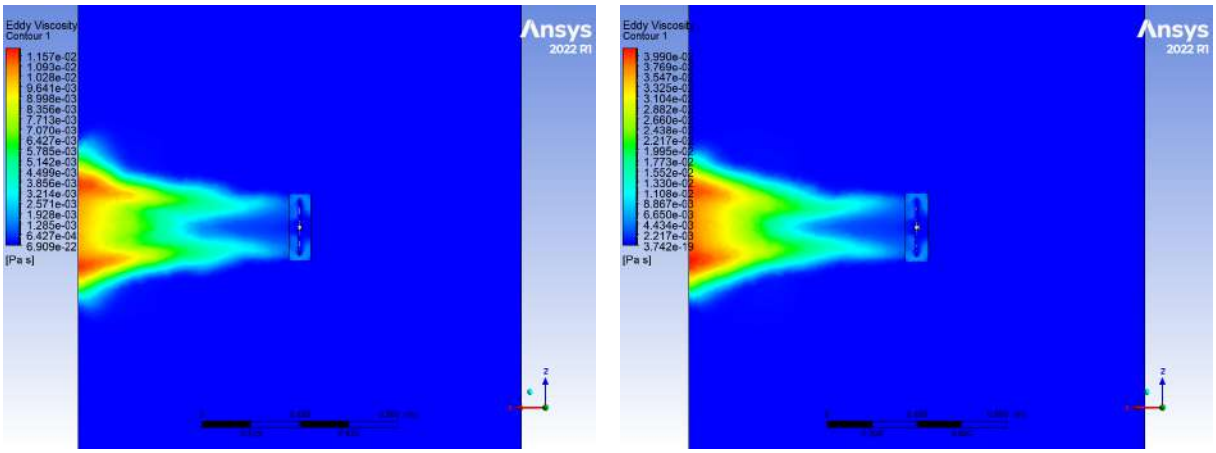

(a) $\Omega = 1759$ RPM. (b) $\Omega = 6218$ RPM.

Figure 4.20: Eddy viscosity distribution. APC 10”x8” Sport.

4.4.5 Unsteady Solution

As detailed in Chapter 2, simulations involving unsteady phenomena require a considerable amount of computational resources, especially at higher rotation rates. To ensure the accuracy of the results, it is recommended to keep the time step at a minimum of 1°-2° (angle of rotation of the propeller) per time step. Consequently, these simulations are typically reserved for scenarios where transient effects are of significant importance.

In order to attest to the accuracy of the steady state simulations, an unsteady simulation was performed with the same mesh and turbulence model mentioned in the previous sections. Considering hovering flight conditions and a propeller rotational velocity equal to 6218 RPM, the time step should be within $2,7 \times 10^{-5}$ and $5,4 \times 10^{-5}$ seconds solving between 1° and 2° per time step. Therefore, the time step chosen was equal to $3,5 \times 10^{-5}$ seconds. Figure 4.21 presents the evolution of thrust and torque in time.

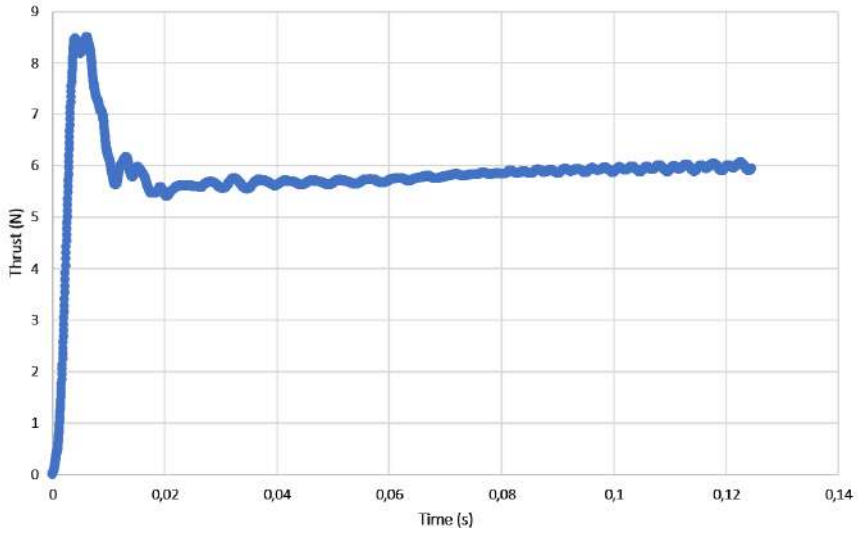

(a) Thrust.

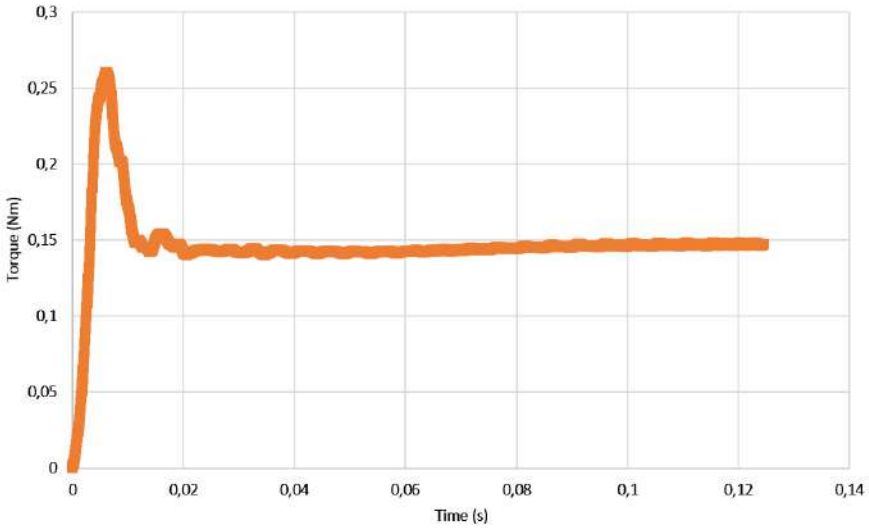

(b) Torque.

Figure 4.21: Transient solution. $\Omega = 6218$ RPM. APC 10"x8" Sport.

It is shown that the simulation covers over 0,12 seconds (over 12 revolutions) of the propeller rotational motion. It is clear how the thrust and torque arrive at an oscillatory regime and they start to stabilize after 0,08 seconds. Table 4.13 presents the comparisons between values of the thrust and torque for the unsteady solution and the results obtained in the steady simulation.

Table 4.13: Steady vs Unsteady flow simulation. $\Omega = 6218$ RPM. APC 10"x8" Sport.

Model	Thrust (N)	$(\%)\epsilon_{thrust}$	Torque (Nm)	$(\%)\epsilon_{torque}$
Steady	6	-4,89	0,148	1,45
Unsteady	5,96	-5,55	0,147	0,67

The analysis reveals that the torque and thrust have negligible variations of less than 0.8% between the steady-state and transient simulations. This indicates that the steady-state approach is a reliable method for propeller performance analysis, providing accurate mean values while significantly reducing computational costs. Upon completing 12 revolutions with the designated time step and starting from a rotational velocity of zero, the computational time surpassed 100 hours while utilizing 12 processors. In contrast, a steady simulation that reached convergence after approximately 2000 iterations lasted only 4 hours.

Chapter 5

Experimental Testing and Validation

This Chapter addresses the experimental aerodynamic performance measurements of the APC 10”$\times$ 8” Sport propeller. The experimental setup used, as well as the testing procedures and data reduction process utilized, are comprehensively explained in detail, all of which are relevant to the propeller in question. The goal was to validate the numerical models studied in the previous chapter.

5.1 Experimental Setup

Thrust measurements were conducted utilizing a force balance as designed and employed in a study authored by M. Borges [39]. The experimental testing was carried out at Instituto Superior Técnico (IST).

The process of constructing the balance was broken down into several different stages, clearly illustrated in the diagram depicted in Figure 5.1.

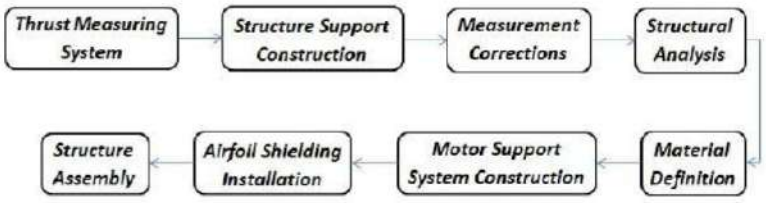

Figure 5.1: Stages of construction of the force balance [40].

These stages are carefully studied and analyzed in the referred study. The final assembly of the force balance is shown in Figure 5.2.

The connection between the motor and propeller has been thoughtfully designed to allow for testing procedures with various motor types. This connection features a cross-shaped configuration that is capable of accommodating motors ranging from 15 to 55 millimeters in diameter size. Figure 5.3 provides a clearer understanding of this structure. It is possible to visualize the cross structure supported by four bolts intersecting with the plate.

Figure 5.2: Force balance at Instituto Superior Técnico.

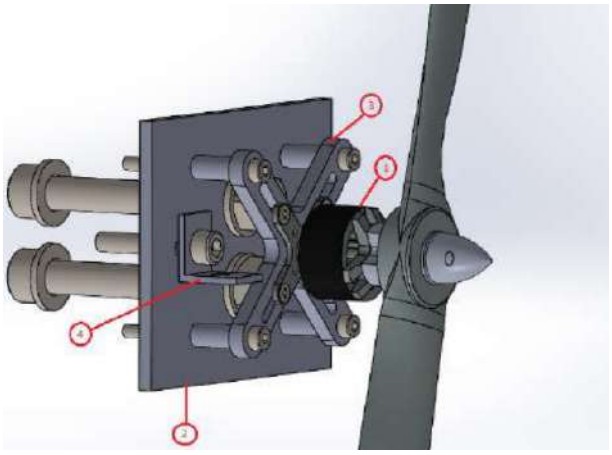

Figure 5.3: Structure for the motor+propeller assembly.

Here is a breakdown of the components enumerated in Figure 5.3:

1. Motor;
2. Support plate;
3. Structural cross;
4. L connection.

To obtain the required data on the propeller's performance, the structure was equipped with the following sensors:

- Load cell;
- Voltage and current sensors;
- RPM sensor.

In the case of the load cell, the Vishay STC Model [41] was chosen. This component is capable of measuring a load up to 5 kg.f and can be used in traction or compression. It also comes with a signal conditioner to amplify the voltage output cell. In the case of the voltage and current sensor, the 60 V version of PitLab 75A [42] was used due to the simplicity of the wiring. In order to measure the RPM, the sensor Vishay CNY 70 [41] was used. A white tape was installed around the diameter of the black motor except for a little angle. When passing through the black part of the motor, the sensor generates a signal with a different frequency. When the change between frequencies is multiplied by 60, the RPM value is obtained.

Additionally, an Electronic Speed Control (ESC) was implemented to regulate and manage the motor's velocity. This device enables speed control through a PMW signal (Pulse Width Modulation). The control process was executed using the LabView® Interface software. The main interface scheme is depicted in Figure 5.4.

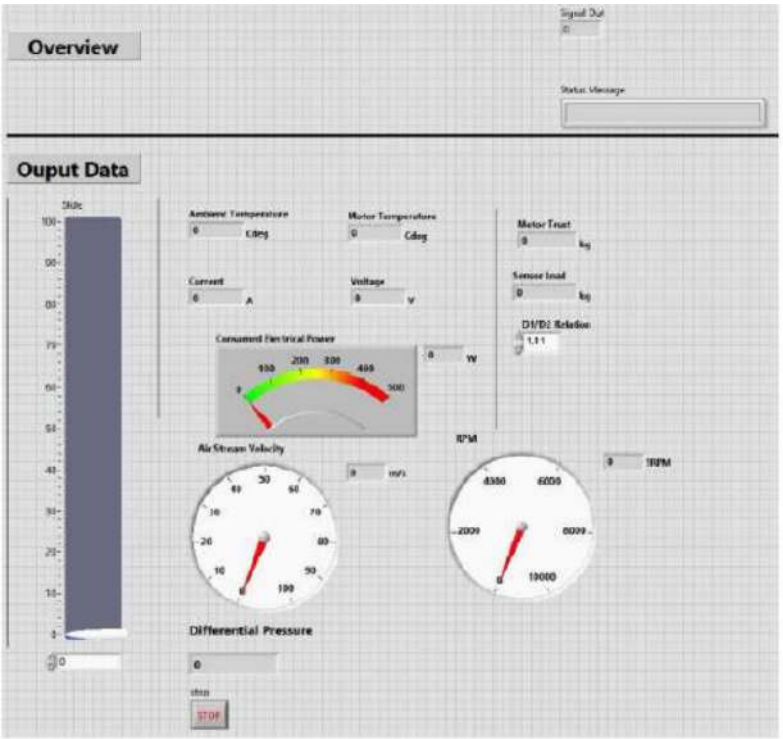

Figure 5.4: LabView® graphical user interface.

This software provides the capability to regulate the motor's throttle level and, correspondingly, control the rotation of the system's motor and propeller. It is important to note that the relationship between the two is directly proportional, allowing for precise adjustments to be made.

5.2 Static Tests

As explained earlier, propeller performance analysis involves evaluating two configurations: static and dynamic conditions. Static conditions refer to situations where there is no income flow on the propeller.

Since the low-speed wind tunnel at the IST Aerospace Engineering Laboratory was out of service, only static tests were conducted. Hence, the propeller APC 10" $\times$ 8" Sport was mounted in combination with the T-Motor AT2317 KV880 model [43], as shown in Figures 5.5 and 5.6, replicating hovering flight conditions.

Figure 5.5: T-Motor AT2317 KV880.

Figure 5.6: T-Motor AT2317 KV880 + APC 10" $\times$ 8" Sport assembly.

In the experimental phase of this study, the main objective is to determine the propeller thrust for hovering flight situations. The experimental tests were carried out using the following steps:

1. Brushless motor (T-Motor AT2317 KV880) and propeller (APC 10" $\times$ 8" Sport) were assembled and mounted onto the force balance;
2. Data acquisition system, computer, and power supply were connected to the test equipment and measurement device;
3. LabView® Interface was opened on the computer;
4. Measurements of the propeller and motor performance were obtained by changing the throttle of the motor in LabView®;
5. Each measurement could only last a maximum of 100 seconds due to the software and structure limitations.

For the current study, the throttle of the motor level ranged from 15% and 60% in small increments (5 to 10 seconds at each level). In the experimental tests, different parameters were analyzed:

- Thrust;
- Electrical power.

As previously stated, data was collected during a 5 to 10-second interval for each motor throttle level. Hence there was some level of uncertainty in the calculations. To address this, the mean and standard deviation values for angular velocity, thrust, and electrical power are included in table 5.1.

Table 5.1: Mean and standard deviation for each throttle of the motor level.

	RPM		Thrust (N)		Electrical Power (W)	
Throttle (%)	Average	Standard Deviation	Average	Standard Deviation	Average	Standard Deviation
22	1714,7	13,11	0,31	0,005	5,30	0,038
25	2358,9	14,11	0,70	0,006	6,36	0,045
29	2958,2	12,84	1,19	0,016	13,63	0,103
33	3495,4	17,35	1,84	0,014	21,61	0,063
38	4014,6	17,88	2,56	0,021	32,49	0,151
43	4506,2	11,81	3,36	0,026	46,13	0,122
48	4959,2	38,03	4,21	0,029	60,59	0,221
54	5604,5	41,67	5,50	0,037	85,07	0,636
59	6212,7	25,10	7,01	0,114	112,01	0,922

It can be seen that for all parameters the standard deviation increases with the throttle level and that the maximum power supplied to the motor exceeded 112 W. In Figure 5.7, it is possible to visualize the graphics with the data acquired on the experiments changing the throttle of the motor level (associated with the change in angular velocity).

In addition, the thrust results from the experimental setup mentioned in the previous Section are compared to CFD simulation results and experimental data from the University of Illinois at Urbana-Champaign [7].

As motor power and propeller speed are increased, the precision and accuracy of data collected at IST may decrease due to calibration challenges and environmental conditions. Factors such as temperature and pressure can significantly impact the recorded data, potentially causing inconsistencies in

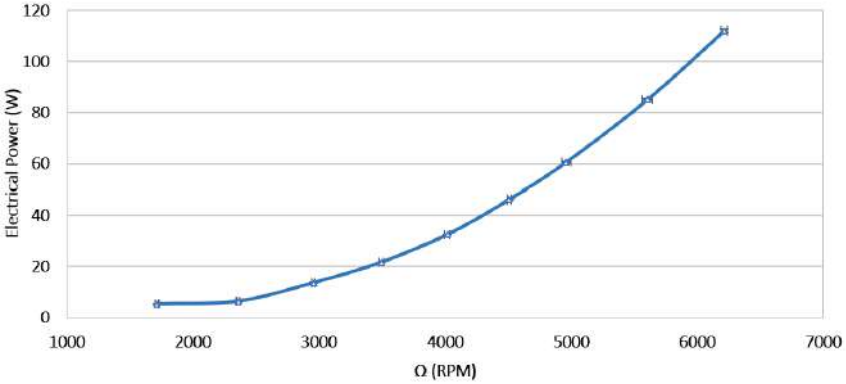

(a) Electrical Power.

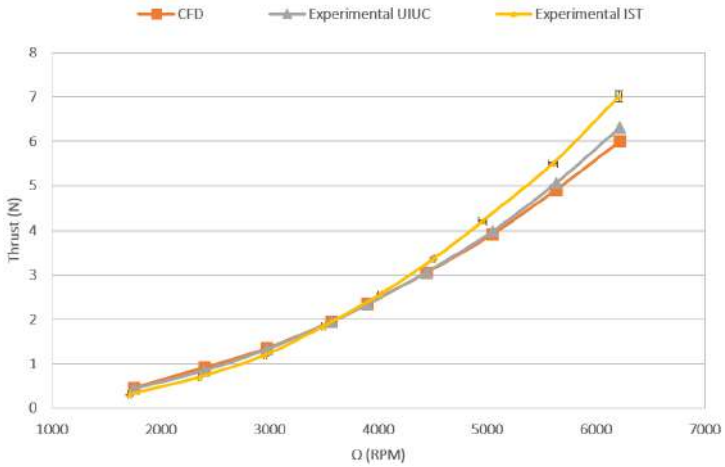

(b) Thrust.

Figure 5.7: Experimental performance. APC 10”x8” Sport.

the values obtained. However, despite these difficulties, the experimental data collected at IST remains valuable and can be validated as it demonstrates similar trends to results obtained from UIUC testing and CFD simulations.

Chapter 6

Conclusions

6.1 Achievements

This study delves into the various techniques utilized for predicting the aerodynamic performance of a drone propeller. These methods can be classified into two groups based on their level of complexity: low-fidelity and high-fidelity numerical analyses.

The study involved two commercial propellers, the APC 14”x13” Sport and APC 10”x8” Sport, under a variety of flight configurations, such as hovering and vertical climb. To obtain thrust and torque, ANSYS® Fluent® and JavaProp software were employed. To ensure the accuracy of the findings, the thrust and torque measurements were compared to the experimental testing conducted at the University of Illinois Urbana-Champaign [7].

A comprehensive computational study was conducted to determine the optimal turbulence model for analyzing propeller performance. The $k-\epsilon$ Standard model was found to provide more accurate results for the APC 14”x13” Sport propeller, while the $k-\omega$ SST model was more effective for the APC 10”x8” Sport propeller. Selecting the most appropriate model depends on the specific flight conditions being analyzed.

In order to reduce numerical errors, a mesh refinement study was conducted on the rotating region of the flow domain surrounding the propeller. Additionally, a sensitivity analysis on the rotating region was performed. Both studies aimed to create a reliable flow model, while also considering the computational time required for simulations.

Vertical climb flight simulations were performed for APC 14”x13” Sport propeller at different rotational and free stream velocities. Based on observations, the CFD simulations yielded consistently accurate results for all flight configurations, except when the rotational propeller velocity decreased, resulting in significant errors. Using the Blade Element Theory in JavaProp software led to the conclusion that the accuracy decreases as the propeller rotating velocity increases.

Hovering flight (no incoming free stream) simulations were conducted for the APC 10”x8” Sport propeller at different rotational velocities ranging from 1759 RPM to 6218 RPM. The CFD simulations showed a maximum discrepancy of -4,89% for the thrust coefficient and -2,84% for the torque coefficient.

Meanwhile, the Blade Element Theory approach had a maximum error of -7,12% for thrust and 7,80% for torque. Additionally, a transient simulation was carried out to investigate the reliability of steady-state simulations. The analysis, conducted at a rotational velocity of 6218 RPM, indicated that there were insignificant variations (less than 0,8%) in the torque and thrust between the steady-state and unsteady-state simulations. While simulating 12 propeller revolutions lasted over 100 hours, a steady simulation took about 4 hours to converge. It was concluded that steady approaches are a reliable method for analyzing propeller performance.

A series of static experimental tests were conducted using a force balance built and calibrated at Instituto Superior Técnico. The tests aimed to evaluate the performance of the APC 10”x8” Sport propeller. The testing results showed a high correlation between the CFD simulations and the experiments carried out at the University of Illinois at Urbana-Champaign (UIUC).

Based on the results obtained, both the low-fidelity and high-fidelity methods have demonstrated a reliable ability to forecast propeller efficiency in various flow and flight scenarios. These findings suggest that either method may be suitable for use in various applications requiring accurate propeller efficiency predictions.

6.2 Future Work

This study has yielded valuable insights into the prediction of drone propeller performance under varying flight conditions. However, there are still several opportunities for further research and development in this field.

1. Enhanced Turbulence Models: to enhance the precision of predictions for regions where flow separation and intricate aerodynamic phenomena take place, further investigation of turbulence models is warranted. Advanced turbulence models such as Large Eddy Simulation (LES) or hybrid RANS-LES models can be scrutinized to identify or formulate more accurate models that are customized to specific flight conditions.

2. Validation and Experimental Studies: to improve the credibility of computational predictions, it is essential to validate them through experiments on a regular basis. One effective way of achieving this is to generate a comprehensive dataset by conducting experiments with a range of propeller designs and sizes, as well as under diverse flight conditions.

3. Aeroacoustic Analysis: Investigating the aeroacoustic aspects of drone propellers is of paramount importance, particularly in metropolitan areas where noise pollution is a significant concern. Future studies could concentrate on predicting and minimizing the noise generated by propellers during various flight modes. This could entail coupling computational fluid dynamics simulations with acoustic models to simulate the noise signature accurately.

In conclusion, the future of drone propeller performance prediction research lies in advancing existing techniques, exploring novel avenues of inquiry, and addressing the ever-evolving challenges of the drone

industry. By prioritizing these areas, researchers can play a vital role in enhancing the efficiency and reliability of drone propulsion systems across a diverse range of scenarios.

Bibliography

[1] S. Farì, “Guidance and Control for a Fixed-Wing UAV,” Ph.D. dissertation, 12 2017. DOI: 10.13140/RG.2.2.24973.28641

[2] H. Sun, H. Yan, M. Hassanalian, J. Zhang, and A. Abdelkefi, “UAV Platforms for Data Acquisition and Intervention Practices in Forestry: Towards More Intelligent Applications,” *Aerospace*, vol. 10, p. 317, 03 2023. DOI: 10.3390/aerospace10030317

[3] M. Merchant and L. Miller, “Propeller Performance Measurement for Low Reynolds Number UAV Applications,” 01 2006. DOI: 10.2514/6.2006-1127

[4] E. V. Loureiro, N. L. Oliveira, P. H. Hallak, F. S. Bastos, L. M. Rocha, and A. C. C. L. R. G. P. Delmonte, “Evaluation of Low Fidelity and CFD Methods for the Aerodynamic Performance of a Small Propeller,” *Aerospace Science and Technology, Volume 108*, 2021.

[5] J. B. Brandt and M. S. Selig, “Propeller Performance Data at Low Reynolds Numbers,” *49th AIAA Aerospace Science Meetings, Orlando, USA*, 2011. DOI: 10.2514/6.2011-1255

[6] J. B. Brandt, “Small-Scale Propeller Performance at Low Speeds,” Master’s thesis, University of Illinois at Urbana-Champaign, USA, 2005.

[7] J. B. Brandt, R. W. Deters, G. K. Ananda, and M. S. Selig. UIUC Propeller Database. https://m-selig.ae.illinois.edu/props/propDB.html/. (accessed: March 2023).

[8] Y.-J. Go, J.-H. Bae, J. Ryi, J.-S. Choi, and C.-R. Lee, “A Study on the Scale Effect According to the Reynolds Number in Propeller Flow Analysis and a Model Experiment,” *Aerospace*, vol. Volume 9, no. 10, 2022. DOI: 10.3390/aerospace9100559

[9] R. W. Deters, G. K. A. Krishnan, and M. S. Selig, “Reynolds Number Effects on the Performance of Small-Scale Propellers,” in *32nd AIAA Applied Aerodynamics Conference, Atlanta, USA*, 2014, p. 2151.

[10] D. Serrano, M. Ren, A. J. Qureshi, and S. Ghaemi, “Effect of Disk Angle-of-Attack on Aerodynamic Performance of Small Propellers,” *Aerospace Science and Technology*, vol. 92, pp. 901–914, 2019. DOI: 10.1016/j.ast.2019.07.022

[11] E. Benini, “Significance of Blade Element Theory in Performance Prediction of Marine Propellers,” *Ocean Engineering*, vol. 31, pp. 957–974, 06 2004. DOI: 10.1016/j.oceaneng.2003.12.001

[12] J. Carroll and D. Marcum, “Comparison of a Blade Element Momentum Model to 3D CFD Simulations for Small Scale Propellers,” *SAE International Journal of Aerospace*, vol. 6, pp. 721–726, 07 2013. DOI: 10.4271/2013-01-2270

[13] D. Wilhelm, “Rotating Flow Simulations with OpenFOAM,” *International Journal of Aeronautical Science & Aerospace Research*, vol. 1, no. 001, 2015.

[14] H. Kutty and P. Rajendran, “3D CFD Simulation and Experimental Validation of Small APC Slow Flyer Propeller Blade,” *Aerospace*, vol. 4, no. 1, 2017. DOI: 10.3390/aerospace4010010

[15] B. W. McCormick, *Aerodynamics, Aeronautics and Flight Mechanics*. John Wiley and Sons, 2nd Edition, 1994, ISBN-13: 978-0471575061.

[16] J. Roskam and C. Lan, *Airplane Aerodynamics and Performance*. DARcorporation, 1st Edition, 1997, ISBN-13: 978-1884885440.

[17] S. Drzewiecki, *Théorie générale de l’hélice: hélices aériennes et hélices marines*. Gauthier-Villars et cie., 1920.

[18] A. Betz, “Schraubenpropeller mit geringstem energieverlust. mit einem zusatz von l. prandtl,” *Nachrichten von der Gesellschaft der Wissenschaften zu Göttingen, Mathematisch-Physikalische Klasse*, vol. 1919, pp. 193–217, 1919.

[19] J. Gorman, S. Bhattacharyya, L. Cheng, and J. P. Abraham, *Applications of Computational Fluid Dynamics Simulation and Modeling*. S. Bhattacharyya, 2022, ISBN-13: 978-1839682476, ch. 2. Turbulence Models Commonly Used in CFD.

[20] J. Blazek, *Computational Fluid Dynamics: Principles and Applications*. Elsevier, 2001, ISBN-13: 978-0-08-099995-1.

[21] D. C. Wilcox *et al.*, *Turbulence Modeling for CFD*. DCW industries La Canada, CA, 1998, ISBN-13: 978-1928729082, vol. 2.

[22] S. B. Pope, “Turbulent flows,” *Measurement Science and Technology*, vol. 12, no. 11, pp. 2020–2021, 2001, ISBN-13: 978-0521598866.

[23] F. Carneiro, L. Moura, P. Costa Rocha, R. Pontes Lima, and K. Ismail, “Application and Analysis of the Moving Mesh Algorithm AMI in a Small Scale HAWT: Validation with Field Test’s Results Against the Frozen Rotor Approach,” *Energy*, vol. 171, pp. 819–829, 2019. DOI: 10.1016/j.energy.2019.01.088

[24] M. Fortin, S. Houde, and C. Deschênes, “Validation of Simulation Strategies for the Flow in a Model Propeller Turbine During a Runaway Event,” *IOP Conference Series: Earth and Environmental Science*, vol. 22, no. 3, p. 032026, mar 2014. DOI: 10.1088/1755-1315/22/3/032026

[25] A. Ghenaiet and A. Halimi, “Aerodynamic Characterization of a High Speed Propeller,” in *Turbo Expo: Power for Land, Sea, and Air*, vol. 45578. American Society of Mechanical Engineers, 2014.

[26] F. Moukalled, M. Darwish, and L. Mangani, *The Finite Volume Method in Computational Fluid Dynamics. An Advanced Introduction with OpenFOAM® and Matlab*. Springer, 2015, ISBN-13: 978-3319168739.

[27] A. Fluent, “15.0, 2013,” *Ansys Fluent Theory Guide*, vol. 15317, pp. 724–746.

[28] APC 14x13 Sport Propeller. https://www.apcprop.com/product/14x13/. (accessed: March 2023).

[29] APC 10x8 Sport Propeller. https://www.apcprop.com/product/10x8/. (accessed: March 2023).

[30] APC Propellers Technical Information. https://www.apcprop.com/technical-information/file-downloads/. (accessed: March 2023).

[31] M. Hepperly. PropellerScanner. http://mh-aerotools.de. (accessed: March 2023).

[32] D. V. Uhlig, “”Post Stall Propeller Behavior at Low Reynolds Numbers”,” Master’s thesis, University of Illinois at Urbana-Champaign, USA, 2007.

[33] C. A. Schneider, W. S. Rasband, and K. W. Eliceiri, “NIH Image to ImageJ: 25 Years of Image Analysis. Nature Methods,” *Nature Methods*, vol. 9, no. 7, pp. 671–675, 2012.

[34] A. Tools. Airfoil Tools Clark-Y. http://airfoiltools.com/airfoil/details?airfoil=clarky-il. (accessed: March 2023).

[35] M. Stajuda, M. Karczewski, D. Obidowski, and K. Jóźwik, “Development of a CFD model for Propeller Simulation,” *Mechanics and Mechanical Engineering*, vol. 20, 2016.

[36] M. Hepperly. JavaProp. http://www.mh-aerotools.de/airfoils/javaprop.htm. (accessed: March 2023).

[37] M. Ol, C. Zeune, and M. Logan, “Analytical/Experimental Comparison for Small Electric Unmanned Air Vehicle Propellers,” in *26th AIAA Applied Aerodynamics Conference, Honolulu, USA*, 2008, p. 7345.

[38] R. Mehdipour, “”Simulating Propeller and Ppropeller-Hull Interaction in OpenFOAM”,” Master’s thesis, Royal Institute of Technology, Stockholm, Sweden, 2013.

[39] M. Borges, “Design of an Apparatus for Wind Tunnel Tests of Electric UAV Propulsion Systems,” Master’s thesis, Instituto Superior Técnico, Portugal, 2015.

[40] N. Moita, “Optimization of the Propeller-Driven Propulsion System for a Small UAV,” Master’s thesis, Instituto Superior Técnico, Portugal, 2018.

[41] V. Intertechnology. https://www.vishay.com/. (accessed: June 2023).

[42] P. I. Electronics. https://www.https://www.pitlab.com/. (accessed: June 2023).

[43] T-Motor. https://store.tmotor.com/. (accessed: May 2023).

Appendix A

Propeller APC 14” $\times$ 13” Sport

r/R	c/R	Beta (º)	x_rotation	y_rotation
0,01	0,13	35,0651	4,5	4,5
0,0848	0,155	33,4148	8,1938	6,1098
0,1352	0,1454	39,553	8,9102	7,8170
0,1857	0,1424	46,2177	9,6714	9,1198
0,2361	0,1428	49,3838	10,1192	9,4343
0,2866	0,1419	47,5591	10,3430	9,2546
0,337	0,1425	44,5754	10,4326	9,1198
0,3875	0,1454	40,8619	10,4326	8,8053
0,4379	0,1492	37,4188	10,3878	8,6256
0,4884	0,1524	34,5253	10,2535	8,2662
0,5388	0,1558	31,8127	10,1192	7,9517
0,5893	0,1578	29,6376	9,7162	7,4126
0,6398	0,158	27,5599	9,0893	6,8735
0,6902	0,1552	25,8922	8,2386	6,2446
0,7407	0,1484	24,4665	7,1640	5,4359
0,7911	0,1371	22,9904	5,7760	4,6722
0,8416	0,1203	21,8799	3,9402	3,6389
0,892	0,0974	20,4448	1,9701	2,3361
0,9425	0,0673	18,4893	-0,7164	0,9434
1	0,0091	14	-5,8208	-1,3927

Table A.1: Geometry data. APC 14” $\times$ 13” Sport.

$\underline{\Omega = 2003}$ RPM

CFD	2003 RPM	
J	c_T	c_Q
0,31	0,1132	0,0128
0,409	0,1059	0,0127
0,467	0,1017	0,0125
0,521	0,0957	0,0124
0,566	0,0904	0,0122
0,669	0,0766	0,0114
0,728	0,0678	0,0108

JavaProp	2003 RPM	
J	c_T	c_Q
0,31	0,0991	0,0126
0,409	0,0947	0,0126
0,467	0,0912	0,0126
0,521	0,0871	0,0125
0,566	0,0833	0,0124
0,669	0,0721	0,0117
0,728	0,0636	0,0109

Experimental (UIUC)	2003 RPM	
J	c_T	c_Q
0,31	0,0994	0,0122
0,409	0,0976	0,0120
0,467	0,092	0,0119
0,521	0,0861	0,0118
0,566	0,0792	0,0114
0,669	0,063	0,0102
0,728	0,0528	0,0092

Table A.2: $\Omega = 2003$ RPM performance results: a) CFD b) JavaProp c) Experimental [7]

$\underline{\Omega = 2508}$ RPM

CFD	2508 RPM	
J	c_T	c_Q
0,286	0,1126	0,0127
0,373	0,1077	0,0127
0,457	0,1009	0,0125
0,541	0,0937	0,0123
0,617	0,0842	0,0118
0,699	0,0725	0,0111

JavaProp	2508 RPM	
J	c_T	c_Q
0,286	0,1000	0,0126
0,373	0,0965	0,0126
0,457	0,0918	0,0126
0,541	0,0854	0,0125
0,617	0,0781	0,0122
0,699	0,0681	0,0113

Experimental (UIUC)	2508 RPM	
J	c_T	c_Q
0,286	0,1087	0,0121
0,373	0,1078	0,0120
0,457	0,1011	0,0121
0,541	0,0923	0,0120
0,617	0,0785	0,0117
0,699	0,0632	0,0101

Table A.3: $\Omega = 2508$ RPM performance results: a) CFD b) JavaProp c) Experimental [7]

$\Omega = 2998$ RPM

CFD	2998 RPM	
J	c_T	c_Q
0,206	0,1145	0,0125
0,277	0,1119	0,0127
0,31	0,1102	0,0127
0,381	0,1056	0,0127
0,412	0,1034	0,0126
0,485	0,0975	0,0125
0,553	0,0922	0,0122
0,617	0,0843	0,0118

JavaProp	2998 RPM	
J	c_T	c_Q
0,206	0,1023	0,0127
0,277	0,1003	0,0126
0,31	0,0991	0,0126
0,381	0,0961	0,0126
0,412	0,0945	0,0126
0,485	0,0899	0,0126
0,553	0,0844	0,0125
0,617	0,0781	0,0122

Experimental (UIUC)	2998 RPM	
J	c_T	c_Q
0,206	0,1133	0,0121
0,277	0,1137	0,0120
0,31	0,1133	0,0120
0,381	0,1098	0,0121
0,412	0,1075	0,0122
0,485	0,1018	0,0122
0,553	0,0928	0,0120
0,617	0,0833	0,0116

Table A.4: $\Omega = 2998$ RPM performance results: a) CFD b) JavaProp c) Experimental [7]

$\Omega = 3508$ RPM

CFD	3508 RPM	
J	c_T	c_Q
0,179	0,1150	0,0125
0,266	0,1122	0,0126
0,355	0,1069	0,0127
0,44	0,1004	0,0125
0,499	0,0958	0,0123
0,533	0,0930	0,0122
0,587	0,0885	0,0120

JavaProp	3508 RPM	
J	c_T	c_Q
0,179	0,1029	0,0129
0,266	0,1007	0,0126
0,355	0,0973	0,0126
0,44	0,0929	0,0126
0,499	0,0888	0,0126
0,533	0,0861	0,0125
0,587	0,0813	0,0123

Experimental (UIUC)	3508 RPM	
J	c_T	c_Q
0,179	0,1205	0,0119
0,266	0,117	0,0118
0,355	0,1137	0,0120
0,44	0,108	0,0122
0,499	0,1017	0,0122
0,533	0,0979	0,0122
0,587	0,0903	0,0120

Table A.5: $\Omega = 3508$ RPM performance results: a) CFD b) JavaProp c) Experimental [7]

Appendix B

Propeller APC 10” $\times$ 8” Sport

r/R	c/R	Beta (°)	x_rotation	y_rotation
0,0228	0,21	30	6,2	2,2
0,0727	0,2112	31,9441	6,4980	2,7572
0,1226	0,1682	33,5217	6,7688	3,164
0,1725	0,1576	41,0842	7,0846	4,068
0,2224	0,154	46,1585	7,2651	4,3844
0,2723	0,1491	44,3843	7,2651	4,4748
0,3222	0,1476	40,6535	7,2651	4,2036
0,3721	0,1497	37,0894	7,1749	3,9776
0,422	0,1541	33,7069	6,9493	3,7516
0,4718	0,1599	30,6702	6,8139	3,3448
0,5217	0,1647	28,5581	6,5883	2,938
0,5716	0,1681	26,4022	6,1821	2,486
0,6215	0,1698	24,7029	5,5955	1,8984
0,6714	0,1685	23,0346	4,8284	1,3108
0,7213	0,1643	21,876	4,0161	0,7684
0,7712	0,1555	20,6432	2,7978	0,0904
0,8211	0,1413	19,4382	1,2635	-0,4068
0,871	0,1221	18,3018	-0,5415	-0,9944
0,9209	0,0958	16,7257	-2,4819	-1,4012
0,9708	0,0604	14,7844	-5,1443	-1,7628
1	0,0159	10,2905	-7,7615	-2,3052

Table B.1: Geometry data. APC 10” $\times$ 8” Sport.

CFD	2003 RPM	
J	c_T	c_Q
0,31	0,1132	0,0128
0,409	0,1059	0,0127
0,467	0,1017	0,0125
0,521	0,0957	0,0124
0,566	0,0904	0,0122
0,669	0,0766	0,0114
0,728	0,0678	0,0108

JavaProp	2003 RPM	
J	c_T	c_Q
0,31	0,0991	0,0126
0,409	0,0947	0,0126
0,467	0,0912	0,0126
0,521	0,0871	0,0125
0,566	0,0833	0,0124
0,669	0,0721	0,0117
0,728	0,0636	0,0109

Experimental (UIUC)	2003 RPM	
J	c_T	c_Q
0,31	0,0994	0,0122
0,409	0,0976	0,0120
0,467	0,092	0,0119
0,521	0,0861	0,0118
0,566	0,0792	0,0114
0,669	0,063	0,0102
0,728	0,0528	0,0092

Table B.2: Performance results: a) CFD b) JavaProp c) Experimental [7]

Appendix C

Matlab® scripts

C.1 main.m

```
1
2  load clarky.dat %load clark-y coordinates
3  load model.txt %load geometry data from the propeller
4
5  [N1,N2]=size(clarky);
6  [N11,N22]=size(clarky);
7  N=N1;%4 zero rows added at the end of every airfoil
8  [M1,M2]=size(model);
9  P=clarky;% First aerofoil
10 Y=zeros(N1*T,3);
11 D=355.6;  %Diameter of the propeller (mm)
12
13 for t=1:T
14 Y(N*t-(N1-1):N*t,3)=model(t,1)*0.5*D; %Places airfoil in correct z-
       coordinate (along the blade)
15 Y(N*t-(N1-1):N*t,1:2)=airfoil_rotation(model(t,3),P*0.5*D*model(t,2),model(
       t,4),model(t,5));%Turns and scales airfoil
16 output = [num2str(Y(N*t,3)) '.txt'];
17 writematrix(Y(N*t-(N1-1):N*t,:), output,'Delimiter','tab');
18 end
```

C.2 airfoil_rotation.m

```
function X=airfoil_rotation(beta,Y,j,i)
b=(90+beta)/180*pi;
Y(:,1)=-(Y(:,1))+0.25*Y(1,1);%Clark-Y center of rotation at 25% chord
X=([cos(b) -sin(b);sin(b) cos(b)]*(Y)')';%Rotation of airfoil.
X(:,2)=X(:,2)+j;%Centers airfoil at thecenter of rotation.
X(:,1)=X(:,1)-i;%Centers airfoil at the center of rotation.
end
```